BRAIN COMMUNICATIONS

Fronto-temporal dementia risk gene *TMEM106B* has opposing effects in different lysosomal storage disorders

Azucena Perez-Canamas,[1,2] Hideyuki Takahashi,[1,2] Jane A. Lindborg[1,2] and Stephen M. Strittmatter[1,2,3]

TMEM106B is a transmembrane protein localized to the endo-lysosomal compartment. Genome-wide association studies have identified *TMEM106B* as a risk modifier of Alzheimer's disease and frontotemporal lobar degeneration, especially with progranulin haploinsufficiency. We recently demonstrated that TMEM106B loss rescues progranulin null mouse phenotypes including lysosomal enzyme dysregulation, neurodegeneration and behavioural alterations. However, the reason whether TMEM106B is involved in other neurodegenerative lysosomal diseases is unknown. Here, we evaluate the potential role of TMEM106B in modifying the progression of lysosomal storage disorders using progranulin-independent models of Gaucher disease and neuronal ceroid lipofuscinosis. To study Gaucher disease, we employ a pharmacological approach using the inhibitor conduritol B epoxide in wild-type and hypomorphic *Tmem106b−/−* mice. TMEM106B depletion ameliorates neuronal degeneration and some behavioural abnormalities in the pharmacological model of Gaucher disease, similar to its effect on certain progranulin null phenotypes. In order to examine the role of TMEM106B in neuronal ceroid lipofuscinosis, we crossbred *Tmem106b−/−* mice with *Ppt1−/−*, a genetic model of the disease. In contrast to its conduritol B epoxide-rescuing effect, TMEM106B loss exacerbates Purkinje cell degeneration and motor deficits in *Ppt1−/−* mice. Mechanistically, TMEM106B is known to interact with subunits of the vacuolar ATPase and influence lysosomal acidification. In the pharmacological Gaucher disease model, the acidified lysosomal compartment is enhanced and TMEM106B loss rescues *in vivo* phenotypes. In contrast, gene-edited neuronal loss of *Ppt1* causes a reduction in vacuolar ATPase levels and impairment of the acidified lysosomal compartment, and TMEM106B deletion exacerbates the mouse *Ppt1−/−* phenotype. Our findings indicate that TMEM106B differentially modulates the progression of the lysosomal storage disorders Gaucher disease and neuronal ceroid lipofuscinosis. The effect of TMEM106B in neurodegeneration varies depending on vacuolar ATPase state and modulation of lysosomal pH. These data suggest TMEM106B as a target for correcting lysosomal pH alterations, and in particular for therapeutic intervention in Gaucher disease and neuronal ceroid lipofuscinosis.

1 Cellular Neuroscience, Neurodegeneration and Repair Program, Yale University School of Medicine, New Haven, CT, USA
2 Department of Neurology, Yale University School of Medicine, New Haven, CT, USA
3 Department of Neuroscience, Yale University School of Medicine, New Haven, CT, USA

Correspondence to: Stephen M. Strittmatter
Department of Neuroscience, Yale University School of Medicine
New Haven, CT, USA
E-mail: stephen.strittmatter@yale.edu

Keywords: lysosome; TMEM106B; Gaucher; neuronal ceroid lipofuscinosis; palmitoyl-protein thioesterase 1

Abbreviations: AAV = adeno-associated virus; CBE = conduritol B epoxide; FTLD = frontotemporal lobar degeneration; GCase = glucocerebrosidase; GD = Gaucher disease; GFAP = glial fibrillary acid protein; NCL = neuronal ceroid lipofuscinosis; PFA = paraformaldehyde; PGRN = progranulin; PPT1 = palmitoyl-protein thioesterase 1; V-ATPase = vacuolar ATPase

Received April 21, 2020. Revised October 2, 2020. Accepted October 9, 2020. Advance Access publication November 16, 2020

Graphical Abstract

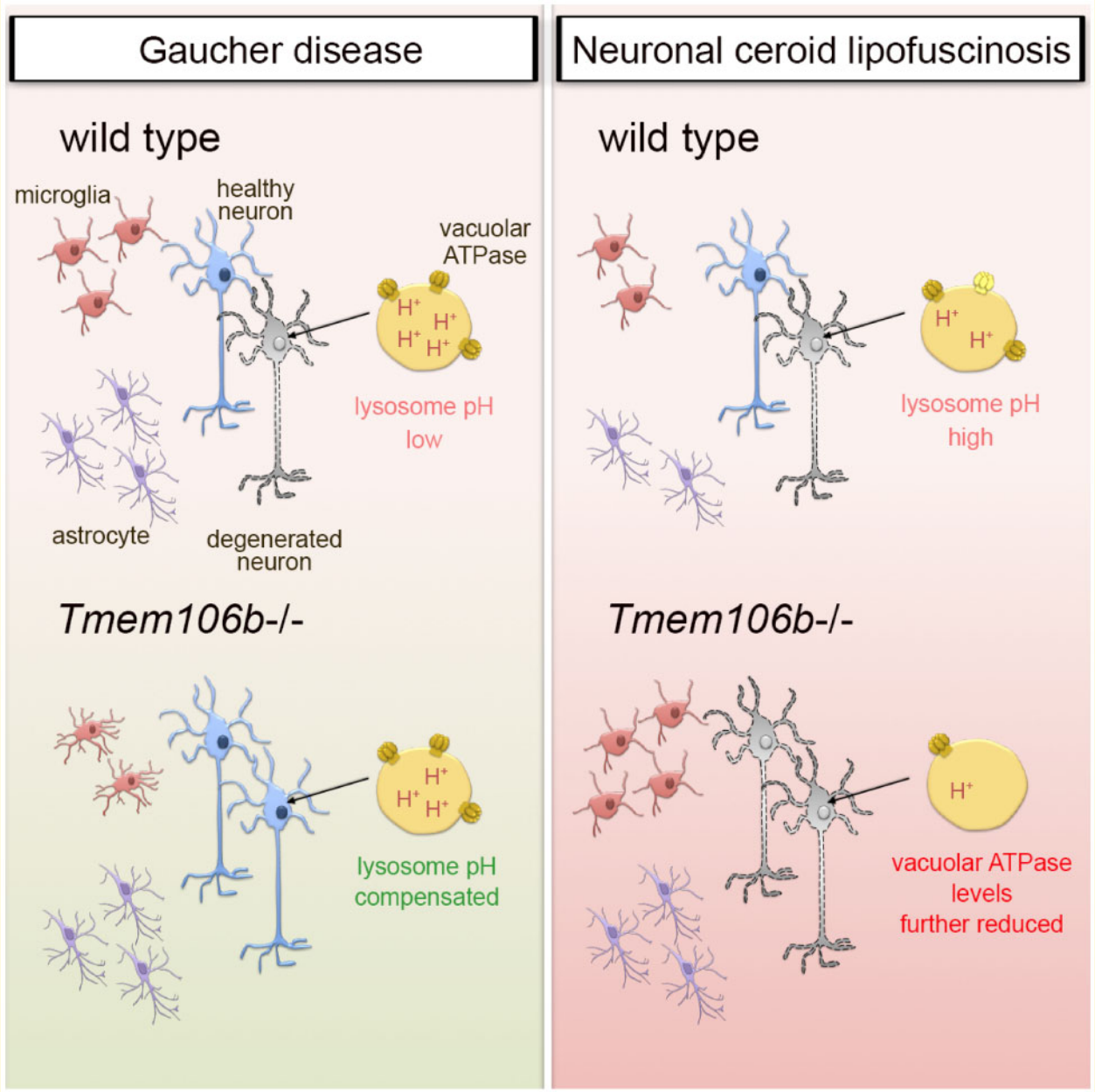

Introduction

Lysosomes are membrane-bound organelles containing more than 50 acid hydrolases that function in the degradation of macromolecules. Lysosomal dysfunction in neurons is closely tied to neurodegeneration and cell death mechanisms (Česen *et al.*, 2012; Nixon and Yang, 2012). Growing genetic and biochemical evidence implicates dysfunction of the endosomal–lysosomal and autophagic lysosomal pathways in the pathogenesis of a number of neurodegenerative disorders, including Alzheimer's Disease, Progranulin (*GRN*) gene-related frontotemporal lobar degeneration (FTLD) and Parkinson's disease (PD) (Nixon, 2013; Ghavami *et al.*, 2014; Menzies *et al.*, 2015).

TMEM106B is a transmembrane lysosomal protein expressed in neurons, glial and endothelial cells (Lang *et al.*, 2012; Busch *et al.*, 2013; Schwenk *et al.*, 2013; Stagi *et al.*, 2014). Genome-wide association study identified *TMEM106B* as a risk modifier of FTLD-TDP (transactivation response element [TAR] DNA-binding protein) (Nicholson and Rademakers, 2016). Single-nucleotide polymorphisms in *TMEM106B* reduce disease penetrance in FTLD-TDP with *GRN* mutations (Van Deerlin *et al.*, 2010; Finch *et al.*, 2011). *TMEM106B* single-nucleotide polymorphisms may also modify the pathological

presentation of Alzheimer's Disease (Rutherford *et al.*, 2012). Several genetic studies have also reported a significant under-representation of the *TMEM106B* protective allele in patients with hippocampal sclerosis (Murray *et al.*, 2014; Nelson *et al.*, 2015). Furthermore, *TMEM106B* genotype predicts the rate of cognitive decline in patients with PD (Tropea *et al.*, 2019).

Haploinsufficiency of progranulin (PGRN) mRNA and protein is a common genetic etiology for FTLD-TDP, a progressive neurodegenerative disease and one of the most common dementias in patients younger than 65 years (Vieira, 2013). We previously characterized the role of TMEM106B depletion in a PGRN-deficient (*Grn*−/−) mouse model (Stagi *et al.*, 2014; Klein *et al.*, 2017). Transcriptomic and proteomic analyses revealed an early lysosomal dysregulation in *Grn*−/− mouse brain, whereas *Tmem106b*−/− mouse brain showed opposite changes in several lysosomal enzymes. Remarkably, TMEM106B deficiency normalized lysosomal protein dysregulation and rescued FTLD-related behavioural deficits and retinal degeneration in *Grn*−/− mice. Mechanistically, TMEM106B interacts with the vacuolar ATPase (V-ATPase), a multimeric pump that transports protons from the cytosol into the lysosomal lumen and maintains pH gradient across the lysosomal membrane. TMEM106B deficiency causes down-regulation of V-ATPase V0 domain, impairment in lysosomal acidification and hence normalizes lysosomal enzyme activity in *Grn*−/− neurons (Klein *et al.*, 2017). TMEM106B also plays a role in the axonal transport of lysosomes (Stagi *et al.*, 2014; Lüningschrör *et al.*, 2020) and myelination (Simons *et al.*, 2017; Feng *et al.*, 2020b; Zhou *et al.*, 2020b).

In contrast to PGRN haploinsufficiency in FTLD-TDP, homozygous null mutations in the *GRN* gene have been identified as a cause of neuronal ceroid lipofuscinosis (NCL), a lysosomal storage disease (Smith *et al.*, 2012). This devastating disease causes blindness, seizures, motor symptoms and early death, and mice lacking PGRN exhibit retinal neurodegeneration (Hafler *et al.*, 2014). A hallmark of NCLs is the aberrant accumulation of autofluorescent pigment in the lysosomal compartment in neuronal cell bodies. Although TMEM106B deficiency rescues certain phenotypes of young *Grn*−/− mice, lipofuscinosis is not altered by TMEM106B levels (Klein *et al.*, 2017). In addition, recent studies have reported severe motor deficits and lysosomal deficits and motor neuronal loss in spinal cord of older *Tmem106b*−/−; *Grn*−/− double-knockout mice and *Grn*−/− mice with alternate *Tmem106b* loss-of-function alleles (Feng *et al.*, 2020a; Zhou *et al.*, 2020a). Thus, the specificity and mechanistic determinants of TMEM106B modulation of neurodegeneration remain unclear.

Genetic studies have also suggested PGRN as a risk factor for the most prevalent lysosomal storage disorder, Gaucher disease (GD) (Jian *et al.*, 2016b). Gaucher disease is caused by loss-of-function mutations in *GBA1*, which encodes the lysosomal enzyme glucocerebrosidase (GCase) (Hruska *et al.*, 2008). The resulting GCase deficiency causes accumulation of the glycosphingolipid glucosylceramide within lysosomes. Gaucher disease is characterized by hepatosplenomegaly, haematological defects and bone disease (Cox and Schofield, 1997; Vitner *et al.*, 2015). The neurological forms, type 2 (acute) and type 3 (chronic), display central nervous system involvement in addition to systemic disease (Vitner and Futerman, 2013). Progranulin directly binds to and functions as a chaperone of the lysosomal enzyme GCase (Jian *et al.*, 2016a,b) and PGRN mutations result in reduced GCase activity (Arrant *et al.*, 2019; Valdez *et al.*, 2019).

Here, we investigate the potential roles of TMEM106B in lysosomal storage diseases in which PGRN is implicated, GD and NCL. We utilize a pharmacological model to induce GD, the GCase inhibitor conduritol B epoxide (CBE), and a genetic model of NCL, *Ppt1*−/− mice. Although TMEM106B depletion protects against neuronal degeneration and certain behavioural abnormalities in GD, TMEM106B deficiency exacerbates Purkinje cell loss and motor performance in *Ppt1*−/− mice NCL model. Mechanistically, TMEM106B may mediate these opposing effects by influencing lysosomal acidification through V-ATPase. Cultured neurons treated with CBE show increased lysosomal acidification as opposed to the decrease reported in *Tmem106b*−/− neurons. On the other hand, CRISPR-cas9 editing of *Ppt1* in cultured neurons confirms impairment of the acidified lysosome compartment. We propose TMEM106B protein as a regulator of lysosomal physiology with TMEM106B/V-ATPase interactions as a potential therapeutic target for certain lysosome-dependent neurodegenerative conditions.

Materials and methods

Mice

Tmem106b−/− and *Grn*−/− mice were generated previously (Klein *et al.*, 2017). *Ppt1*−/− mice (Gupta *et al.*, 2001) were kindly provided by Dr. Sreeganga Chandra. All mice were maintained on a 12-h light–dark schedule with access to standard mouse chow and water *ad libitum*. Yale Institutional Animal Care and Use Committee approved all animal studies. Both male and female mice were included in the studies, unless otherwise specified.

CBE treatment in mice

In order to induce GD, wild-type (WT) and *Tmem106b*−/− mice were treated with CBE (Millipore, 234599), which is an irreversible inhibitor of GCase (Kanfer *et al.*, 1975). In cohort 1, 2-month-old mice were injected i.p. with 50 mg of CBE per kilogram body weight or vehicle (PBS) per day for 30 days. Since no

sign of pathology was observed using this dose, the amount of drug was increased to 100 mg CBE per kilogram body weight or vehicle (PBS) per day for 15 additional days, when some mice started to show body weight loss and tremors (data not shown). This cohort included males and females ($n = 5$–6 mice per group). In cohort 2, 2-month-old WT and *Tmem106b*−/− females directly received 100 mg CBE per kilogram body weight or vehicle (PBS) per day for 40 days. No poor body condition or apparent signs of motor impairment were observed at the end point of this treatment ($n = 6$–8 mice per group). The second cohort was sacrificed prior to systemic signs in order to allow optimal tissue collection and to assess neurodegeneration prior to and separate from any consequence of general decline.

Immunoprecipitation

The brains were dissected out from male 6- to 7-month-old WT and *Tmem106b*−/− mice and homogenized in five-fold volume of ice-cold Tris-buffered saline with Tween-20 (50 mM Tris-HCl, pH 7.4, 150 mM NaCl, 1% Trion X-100) supplemented with cOmplete Mini (Roche). After ultracentrifugation at 100,000 × *g* for 30 min at 4°C, the supernatant was pre-cleared with Protein A-Sepharose CL-4B (GE Healthcare 17-0780-01) for at least 3 h at 4°C. The pre-cleared lysate was incubated overnight at 4°C with anti-TMEM106B antibody (Abcam ab140185) that is covalently conjugated with Protein A-Sepharose CL-4B using BS^3 (ThermoScientific 21580). The immunoprecipitates were washed six times with ice-cold Tris-buffered saline with Tween-20 and proteins were eluted with 2× Laemmli buffer without 2-mercaptoethanol on ice for 50 min.

Immunofluorescence

For CBE and double-knockout *Ppt1*−/−; *Tmem106b*−/− cohorts, mice were perfused in PBS and brains were immediately post-fixed in 4% paraformaldehyde (PFA) for 24 h at 4°C. Coronal (for CBE cohort) and sagittal (for double-knockout *Ppt1*−/−; *Tmem106b*−/− cohort) 40 μm free-floating sections were prepared using a vibratome (Leica WT1000S). Sections were blocked with 1% bovine serum albumin (Sigma), 1% Triton X-100 in PBS for 1 h, followed by incubation with primary antibody for 2 days at 4°C. The following primary antibodies were used: mouse anti-NeuN (Millipore, MAB377, 1:200), rabbit anti-Iba1 (Wako, 019-19741, 1:250), rat anti-CD68 (AbD Serotec, MCA1957, 1:1000), rabbit anti-glial fibrillary acid protein (GFAP) (Dako, Z-0334, 1:1000), rat anti-Lamp1 (Santa Cruz, 1:250, sc-199929) and rabbit anti-Calbindin D28k (Invitrogen, 711443, 1:100). The sections were washed three times with PBS and incubated in secondary fluorescent antibody (Invitrogen Alexa Fluor, 1:1000) overnight at 4°C. For the Iba1 staining in the *Ppt1*−/− mice, autofluorescence was quenched by treating the stained sections with 10 mM $CuSO_4$ in ammonium acetate for 15 min (Schnell *et al.*, 1999). Typically, a total of four images from two sections per each mouse were captured using LSM800 confocal microscopy with a 10 or 40× objective lens or Zeiss AxioImager Z1 epifluorescence microscopy with a 5× objective lens (for Calbindin). Images were analysed using ImageJ (version 1.50i) software with a single automated macro-script to quantitate areas and intensity. Imaging and quantification were performed without the knowledge of genotype or treatment.

For double-knockout *Grn*−/−; *Tmem106b*−/− cohort, immunohistochemistry and image quantification were performed as reported previously (Takahashi *et al.*, 2017) with modifications. The fixed brain hemispheres from 11-month-old WT, *Grn*−/−, *Tmem106b*−/− and *Grn*−/−; *Tmem106b*−/− mice (both male and female with approximate ratio of 1:1) were embedded in 10% gelatin (Sigma G1896) and fixed in 4% PFA (Sigma 158127) for another 3 days at 4°C. Sagittal 50 μm sections were prepared using a Leica WT1000S vibratome. For GFAP/NeuN staining, two free-floating sections (approximately lateral 1.1 and 1.3 mm) were used. For pTDP-43/TDP-43 staining, one free-floating section (approximately lateral 1.2) was used and heat-mediated antigen retrieval was performed in 10 mM citrate buffer (pH = 6.0) for 30 min at 95°C. The sections were permeabilized and blocked with 10% normal donkey serum, 0.2% Trion X-100 in PBS for 1 h at room temperature (RT), followed by incubation in primary antibody in 1% normal donkey serum, 0.2% Triton X-100 in PBS overnight at RT. The following primary antibodies were used: chicken anti-GFAP antibody (Abcam, ab4674, 1:500), rabbit anti-NeuN antibody (Abcam, ab177487, 1:500), mouse anti-phospho-TDP-43 (pS409/410) antibody (COSMO BIO, TIP-PTD-M01, 1:500), rabbit anti-TDP-43 antibody (Abcam, ab133547, 1:340). The sections were washed three times with PBS and incubated in Alexa Fluor secondary antibody (ThermoFisher, all 1:500) in 1% normal donkey serum, 0.2% Triton X-100 in PBS for 3 h at RT. To quench autofluorescence, the sections were incubated in 10 mM $CuSO_4$ in 50 mM ammonium acetate (pH = 5.0) for 15 min (Schnell *et al.*, 1999).

For GFAP staining, the images were taken using the Zeiss AxioImager Z1 epifluorescence microscopy with a 5× objective lens. For NeuN staining, the single-plane images were taken using LSM800 confocal microscopy with a 10× objective lens and 3 × 3 tile scan function in Zen software. For pTDP-43/TDP-43 staining, the single-plane images were taken using LSM800 confocal microscopy with a 20× objective lens.

Quantitative analyses of the GFAP/NeuN images were performed using Fiji/ImageJ (Version 1.0). All images were uniformly thresholded and binarized. GFAP area was calculated using 'analyse particle' function. The number of NeuN+ cells was calculated using 'analyse particle' function with 'watershed' algorithm after specifying the

particle size and ROI (0.6 mm × width of cortical layers). The mean of two sections was used to represent for each animal. The number of pTDP-43 inclusions in in the motor cortex was examined manually under LSM800 confocal microscopy with a 20× objective lens and the number of the inclusions in the hypothalamus was examined manually using three confocal images with high number of the inclusions and the mean was used to represent for each animal. All procedures were performed by an investigator who was blinded to the genotypes.

For spinal cord staining, 9-month-old WT and *Tmem106b−/−* mice (n = 5 mice per group) were perfused in 4% PFA and spinal cords were dissected and immediately post-fixed in 4% PFA for 24 h at 4°C. Spinal cords were cryoprotected in 30% sucrose. Thirty micron transverse sections from the lumbar enlargement were prepared using a cryostat (Leica CM1850). Six to eight sections per mouse were blocked with 1% bovine serum albumin (Sigma), 1% Triton X-100 in PBS for 1 h, followed by incubation with primary antibody (rat anti-Lamp1, Santa Cruz, sc-199929, 1:250; rabbit anti-GFAP, Dako, Z-0334, 1:1000) and overnight at 4°C. The sections were washed three times with PBS and incubated in secondary fluorescent antibody (Invitrogen Alexa Fluor, 1:1000) overnight at 4°C. A total of eight images per mouse were acquired using a Leica TCS SP8 confocal. Images were analysed using ImageJ (version 1.50i) software with a single-automated macroscript to quantitate areas and particle number. Imaging and quantification were performed without the knowledge of genotype.

Brain homogenization and immunoblots

For immunoblot, brain cortex was homogenized in RIPA buffer (50 mM Tris, 150 mM NaCl, 1 mM EDTA, 0.5% sodium deoxycholate, 1% Triton X-100, 0.1% SDS) supplemented with PhosSTOP and 1× cOmplete Mini protease inhibitor cocktail (Roche). BCA assay (ThermoFisher Scientific) was used to determine the protein concentration in the RIPA soluble fraction. Proteins in the RIPA soluble fraction were resolved by SDS-PAGE using precast 4–20% Tris-glycine gels (Bio-Rad) and transferred onto nitrocellulose membranes (Invitrogen) with an iBlot Dry Blotting System (Invitrogen). Membranes were incubated in blocking buffer (Rockland, MB-070-010) for 1 h at RT and then in primary antibodies overnight at 4°C. The following primary antibodies were used: mouse anti-ATP6AP1 (Santa Cruz, 85.1, sc-81886, 1:500), rabbit anti-ATP6V1A (GeneTex, GTX110815, 1:500), rabbit anti-ATP6v0a1 (Synaptic Systems, 109003, 1:500), rabbit anti-TMEM106B (Abcam, ab140185, 1:1000) and mouse anti-β-actin (Sigma, A1978, 1:2000). Membranes were washed three times with Tris-buffered saline with Tween-20. Secondary antibodies were applied for 1 h at RT (Li-Cor Biosciences, 1:10 000 donkey anti-mouse, donkey anti-rabbit, donkey anti-rat and donkey anti-goat, IRDye 680 or 800). Membranes were then washed and proteins were visualized using an Odyssey Infrared imaging system (Li-Cor Biosciences). Immunoreactive bands were quantified using ImageJ (version 1.50i).

Primary neuronal cultures

Primary cortical cultured neurons were prepared from E16-17 WT embryos as reported previously (Hu *et al.*, 2010) and plated onto PDL-coated 96-well plates (20 000 cells/well) and 15-mm glass coverslips. Neurons were maintained in Neurobasal-A media (Gibco) supplemented with B27 (Gibco). For CBE treatment, seven DIV neurons were treated with 200, 500 or 1000 μM CBE for 7 days. Conduritol B epoxide was added to the media every other day.

DNA constructs

The SpCas9 (pX551) and single-guide RNA (sgRNA, pX552) expression plasmids developed by the Zhang lab (Swiech *et al.*, 2015) were obtained from Addgene. To generate *Gba1* and *Ppt1* sgRNA, 20-nt target sequences were chosen using the CRISPR design tool (https://portals.broadinstitute.org/gpp/public/analysis-tools/sgrna-design). sgRNA sequences were selected to precede a 5′-NGG protospacer-adjacent motif sequence and prioritized based on minimal off-target effects. The primers used to design the sgRNA targets are as follows: Gba1-1 (5′–3′) ACCCGTTACGAGAGCACTCGACG; Gba1-2 (5′–3′) AC CGGATAACTGGAAGTCGTTAG; Ppt1-1 (5′–3′) ACCT GTTAATGTCCAAGTCAACA; Ppt1-2 (5′–3′) ACCCCAT GCCAGATCACCAGCGG. To generate sgRNA-expressing constructs, pX552 was digested using SapI Fast Digest (ThermoFisher Scientific, D1934) and annealed oligos were ligated using T7 DNA Ligase (NEB, M0318). Transformation was performed using One-Shot Stbl3 Chemically Competent *Escherichia coli* (Thermo, 737303). Following maxi prep (Qiagen, 12662), Sanger sequencing confirmed correct sgRNA insertion using the U6 promoter-sequencing primer (5′–3′) GAGGGCCTA TTTCCCATGATTC.

Adeno-associated virus production

Adeno-associated virus (AAV) particles were produced as described previously (Konermann *et al.*, 2013). Briefly, HEK293T cells were maintained in DMEM (Gibco, 11965-092) supplemented with 10% fetal bovine serum (Gibco, 10437028) and 1% penicillin/streptomycin (Gibco, 15140-122). Cells were passaged the day before transfection at a density of 10^7 cells per 15 cm plate and were transfected at approximately 80% confluency. For AAV production, 18 μg of DF6 helper plasmid, 6 μg of sgRNA expression plasmid and 6 μg of 2/1 serotype packaging plasmid were combined in 3 ml of serum-free DMEM. After addition of 150 μl of the transfection reagent polyethylenimine (Polysciences Inc., 23966-1), the

DNA:PEI transfection mixture was incubated at RT for 15 min before adding it to HEK293T cells contained in supplemented DMEM. Transfection supernatant was collected 72 h later, filtered using a 0.22-μm cellulose acetate filter (Corning, 430769), and stored at −80°C. Viral titers were determined using iQ SYBR Green Supermix (Bio-Rad, 1708882) and quantitative PCR (Bio-Rad CFX96). Samples were compared against a standard curve derived from a virus of known titer diluted from 10^{13}–10^{8} copies/ml.

Adeno-associated virus infection in neuronal cultures

Three DIV cortical cultured neurons were co-transduced with AAV2/1-cas9 and AAV2/1-sgRNA for *Ppt1*. Neurons transduced with AAV2/1-cas9 were used as a control. Briefly, 50 μl of AAV2/1 was added to each well. The average virus titer was 10^{7}–10^{9} GC/50 μl. Media was partially changed and fresh Neurobasal media was added 48 h after infection. Neurons were analysed 2 weeks after infection. Media was partially changed once a week.

LysoTracker Red DND-99 staining

Neurons plated on PDL-coated 96-well plates were stained with LysoTracker Red DND-99 (Invitrogen, L7528, 100 nM) for 10 min, washed once with Neurobasal media and then immediately imaged as described previously (Klein *et al.*, 2017). MAP2 staining was performed with the same batch of neurons prepared for LysoTracker staining. Neurons were fixed with 4% PFA for 12 min and blocked with 2% bovine serum albumin, 0.1% Triton X-100 in PBS for 1 h, followed by incubation with anti-MAP2 antibody (Millipore, AB5622, 1:1000) overnight at 4°C. After washing the plates three times with PBS, neurons were incubated in Alexa Fluor 488 donkey anti-rabbit antibody (Invitrogen, 1:1000, A11034) for 1 h. Images of LysoTracker and MAP2 staining were automatically taken using ImageXpress Micro XLS (Molecular Devices) (objective lens, 40×). LysoTracker-positive area, mean fluorescence intensity and integrated fluorescence intensity and MAP2-positive areas were analysed using ImageJ (version 1.50i). A threshold for LysoTracker and MAP2 images was applied to quantify intensity and positive area.

Deoxyribonucleic acid editing confirmation using T7EI enzyme

Deoxyribonucleic acid (DNA) was extracted from cultured neurons using QuickExtract DNA Extraction Solution (Epicentre, QE09050). Experimental target site was amplified by PCR using KAPA HiFi HotStart PCR Kit (Kapa Biosystems, KK2501) in a C1000 Touch Thermal Cycler system (Bio-Rad). The following primer sequences, designed using the PrimerQuest Tool (IDT, http://www.idtdna.com/PrimerQuest), were used for *Ppt1* sg1: GGGAAGAACATGATGGAGGTAA (sense), GGGT GGAGAGAGATGATTTAGTG (antisense); and for *Ppt1* sg2: AGAAGGCAAAGTTCCGTAGG (sense), TCACACC TGAGGCTCTATCT (antisense).

Then the Alt-R Genome Editing Detection Kit with T7 endonuclease I (T7EI) (IDT, 1075932) was used to determine on-target genome editing and estimate editing efficiency by following the manufacturer's instructions. Digestion was visualized in a 1% agarose gel.

Ribonucleic acid extraction and quantitative real-time PCR

Ribonucleic acid (RNA) was isolated from cortical cultured neurons using Trizol reagent (Invitrogen, 15596026) extraction and Purelink RNA kit (Ambion, 10296010). Retrotranscription to first strand cDNA was performed using Maxima H Minus First Strand cDNA Synthesis Kit with dsDNase (ThermoFisher Scientific, K1681). The TaqMan gene expression assay and iQ supermix (Bio-Rad, 170-8862) were used for PCR amplification and real-time detection of PCR products. The following probes were used: *Ppt1* (Mm00477078_m1) and *Gapdh* (Mm99999915_g1) from ThermoFisher Scientific. Real-time quantitative PCR was performed using the C1000 Thermal Cycler and quantified using CFX96 Real-Time System (Bio-Rad). *Ppt1* mRNA expression values were normalized to the *Gapdh* expression level.

Behavioural tests

Mice were allowed to habituate in the testing room for at least 1 h prior to initiating various tests. All behavioural experiments were conducted and analysed by personnel unaware of genotype and treatment group.

Rotarod

Motor testing was performed with an accelerating rotarod apparatus (Columbus Instruments), on which the mice were trained for 2 days at a constant speed: four times at 4 rpm for 1 min on the first day and four times at 8 rpm for 1 min on the second day. On the third day, the rotarod was set to progressively accelerate from 4 to 40 rpm over 5 min, and the mice were tested four times. During the accelerating trials, the latency to fall from the rod was measured.

Elevated plus maze

The elevated plus maze was performed as described by Klein *et al.* (2017). Briefly, mice were individually placed at the centre of the apparatus and behaviour was recorded for 10 min. Between trials, all arms were wiped with 70% ethanol and allowed to dry. Behaviour was video-recorded (JVC Everio, Yokohama, Japan) and tracked by Panlab (Barcelona, Spain) Smart software.

Open field

The open-field test was performed as describe by Klein *et al.* (2017). Briefly, mice were individually placed in the centre of a 50-cm-wide × 50-cm-long × 40-cm-high arena with an open top. Mice were allowed to explore and move freely for 10 min. Total distance travelled was assessed with the Panlab software described above. The box was cleaned with 70% ethanol between trials.

Novel object recognition

The novel object recognition test was performed as described by Salazar *et al.* (2017) with modifications. After a 1-h habituation period, an 8-min acquisition trial was conducted with two identical objects. Mice were randomly assigned to access either two 15-ml conical tubes with blue caps or two wrapped 5-ml plastic syringes (label side down) placed 1 in from the edge the long axis of the cage. The test trial was performed 1 h after the acquisition period. Each mouse was exposed to one 15-ml conical tube with blue cap and one wrapped 5-ml plastic syringe (label side down), wherein one was familiar and one novel. Mice were allowed to explore the cage for 5 min. All trials were recorded using a videocamera (Canon FS400). Orofacial exploration, defined as whisking or sniffing near the objects, was quantified for each object until a combined total of 30-s exploration was reached.

Wire hang

Mice were individually positioned in the centre of a metal grid and then the grid was inverted. The grid was placed at a 40-cm height. The latency to fall over the course of two trials (>1 min rest between each trial) was measured. Trials were concluded for 2 min if a mouse was still hanging. For each mouse, the longest hang time was selected.

Statistical analysis

Two-tailed unpaired *T*-test (for simple comparisons), One-way ANOVA with Tukey's correction (for multiple comparisons), Two-way ANOVA with Sidak's correction (for NOR test) and correlation analysis were performed using Prism (version 7.0a) software. Based on the previous studies, Gaussian distributions were assumed. Data are shown as mean ± SEM. Specific *N* values reflecting different mice are indicated by separate dots on each figure. Data are reported as statistically significant for $P < 0.05$ ($^{*}P < 0.05$; $^{**}P < 0.005$; $^{***}P < 0.001$).

Data availability

The data supporting this study are available in the manuscript and Supplementary Material. Raw data will be made available on request following publication. Summary statistics including exact *P*-values, *F*-values and degrees of freedom are included in the Supplementary Material (Supplementary Table 1).

Results

Hypomorphic *Tmem106b* allele with variable rostral–caudal effects and PGRN interaction

The *Tmem106b*−/− mice are generated based on a gene trap insertion (Klein *et al.*, 2017). Although most protein expression is lost, a sensitive immunoprecipitation/blot combination experiment demonstrates a small (~10%) residual amount of immunoreactive TMEM106B protein in the *Tmem106b*−/− brain (Supplementary Fig. 1A). The identity of TMEM106B peptides accounting for the faint immunoreactivity was verified by liquid-chromatography-mass-spectrometric characterization of tryptic fragments (data not shown). Thus, the *Tmem106b*−/− gene trap line is a hypomorph, consistent with recent description (Zhou *et al.*, 2020a). As reported previously, and of greatest relevance for this study, this line shows no significant increase in astrocytosis in the cerebral cortex or hippocampus (Supplementary Fig. 1B and C) and no cortical neuronal loss at 11 months of age (Supplementary Fig. 1D and E). With regard to an interaction of the hypomorphic *Tmem106b* allele with PGRN deficiency in the forebrain, the *Tmem106b* genotype has no detectable effects on GFAP immunoreactive area or neuronal loss. In addition, we found prominent phospho-TDP-43 inclusions in the hypothalamus, but no other regions of the forebrain, of 11-month-old *Grn*−/− mice, which are decreased by TMEM106B reduction (Supplementary Fig. 1F and G), consistent with the rescue of 9-month-old retinal neurodegeneration (Klein *et al.*, 2017).

In more caudal regions of the central nervous system, complete elimination of TMEM106B protein with CRISPR-cas9 technique causes spinal cord motoneuron vacuolation (Lüningschrör *et al.*, 2020), and synergizes with PGRN loss to create a lethal phenotype by 5 months of age characterized by spinal cord pathology (Feng *et al.*, 2020a; Zhou *et al.*, 2020a). In contrast, the hypomorphic gene trap allele exhibits mild anti-LAMP1-positive lysosomal vacuolization of motoneuron initial segments at 9 months of age (Supplementary Fig. 2A–C) with mild spinal cord astrocytosis (Supplementary Fig. 2D and E), but there is no motor phenotype even at 20 months of age (data not shown). The hypomorphic *Tmem106b*−/− mice lacking PGRN survive until 11 months of age, but then develop a rapidly progressive lethal motor syndrome with ataxia and weakness, consistent with a recent report (Zhou *et al.*, 2020a). At 11 months of age, the double knockout *Grn*−/−; *Tmem106b*−/− brainstem shows significantly greater astrocytosis than the *Grn*−/− samples (Supplementary

Fig. 2F and G). Overall, TMEM106B loss-of-function and its interaction with PGRN are sensitive to residual protein amounts, to assay and to central nervous system region.

TMEM106B loss rescues neuronal degeneration and microgliosis induced by GCase inhibition

In order to study the role of TMEM106B in GD, we induced the disease pharmacologically. Conduritol B epoxide is a covalent active site-directed inhibitor of GCase that recapitulates neuronopathic GD (Kanfer *et al.*, 1975; Farfel-Becker *et al.*, 2011). Two cohorts of WT and *Tmem106b−/−* mice received daily i.p. injections of CBE at different doses (Fig. 1A). First, we focused on analysing neuronal degeneration in layer V of the cortex (Vitner *et al.*, 2014; Rocha *et al.*, 2015). NeuN (Neuronal Nuclei) staining confirmed CBE-induced neuronal death in WT mice, whereas *Tmem106b−/−* mice show resistance to cell loss in both cohorts (Fig. 1B and C). In parallel to neuronal degeneration, CBE treatment induces an increase in the number and activation of microglial cells (Vitner *et al.*, 2014; Rocha *et al.*, 2015), measured by Iba1 and CD68, which is partially rescued in *Tmem106b−/−* mice (Fig. 2). These data indicate that TMEM106B depletion is protective against CBE-induced neuronal loss and microglia activation.

CBE-induced astrocyte proliferation is not recovered by TMEM106B loss

Astrocyte activation is a known feature of GD, and we assessed this feature in the same cohorts. Glial fibrillary acid protein staining shows a robust increase in astrocyte number in layer V of the cortex in both WT and *Tmem106b−/−* mice (Supplementary Fig. 3A and B), indicating that TMEM106B depletion does not protect against astrocytosis induced by CBE. Interestingly, GFAP-positive cells show a prominent signal for the lysosomal marker Lamp1, which we designated as 'Lamp1 rings' (Supplementary Fig. 3C). These Lamp1 rings do not

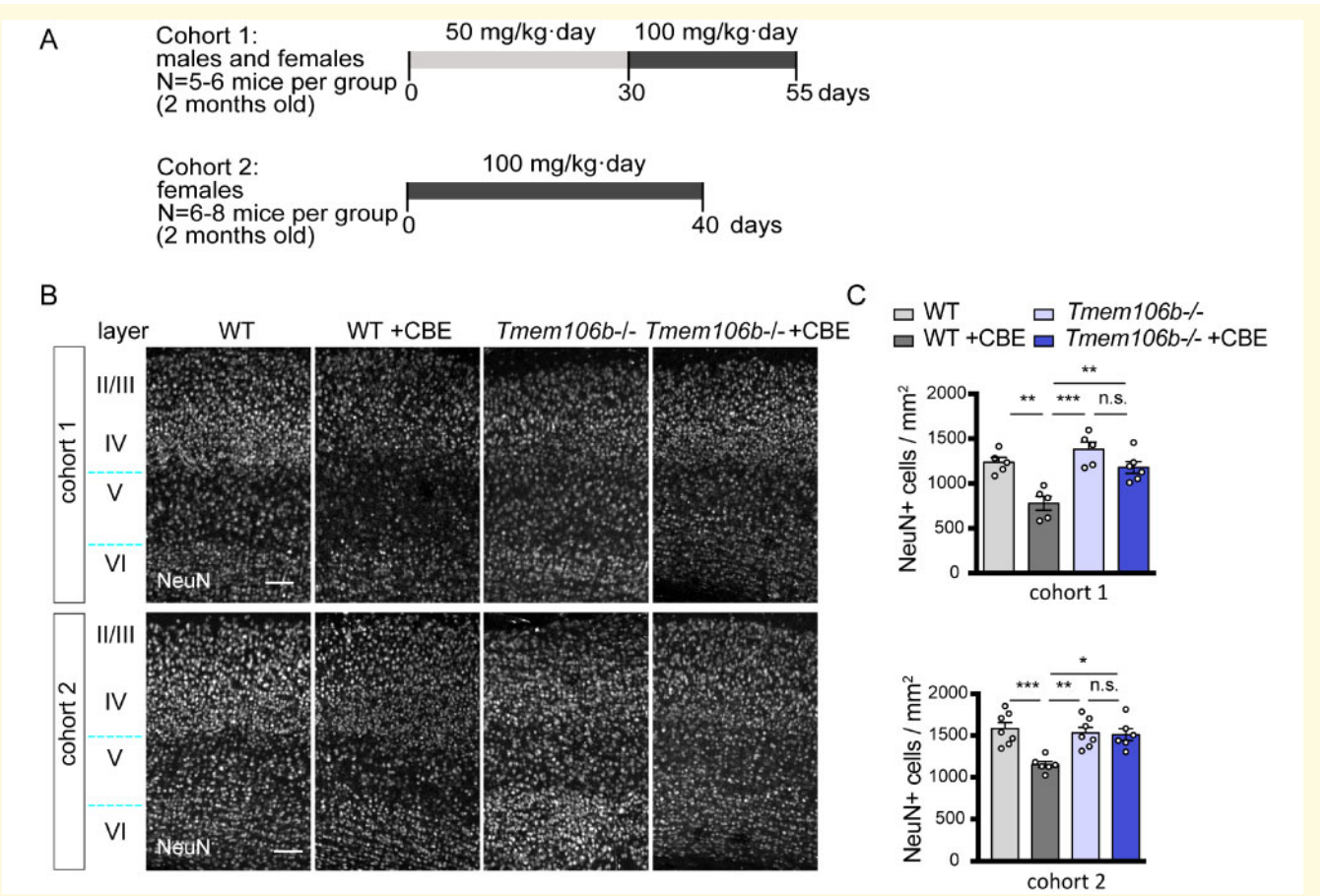

Figure 1 TMEM106B deficiency protects against neuronal death induced by CBE. (**A**) Schematic representation of experimental design. (**B**) Representative images of cortex in WT and *Tmem106b−/−* mice from cohort 1 (top panels) and cohort 2 (bottom panels), treated or not with CBE, stained with anti-NeuN antibody (neurons). Blue lines indicate layer V. Scale bars = 100μm. (**C**) Graphs show mean ± SEM of number of positive cells or area in the layer V of the cortex. For cohort 1, $n = 5–6$ mice per group; for cohort 2, $n = 6–8$ mice per group

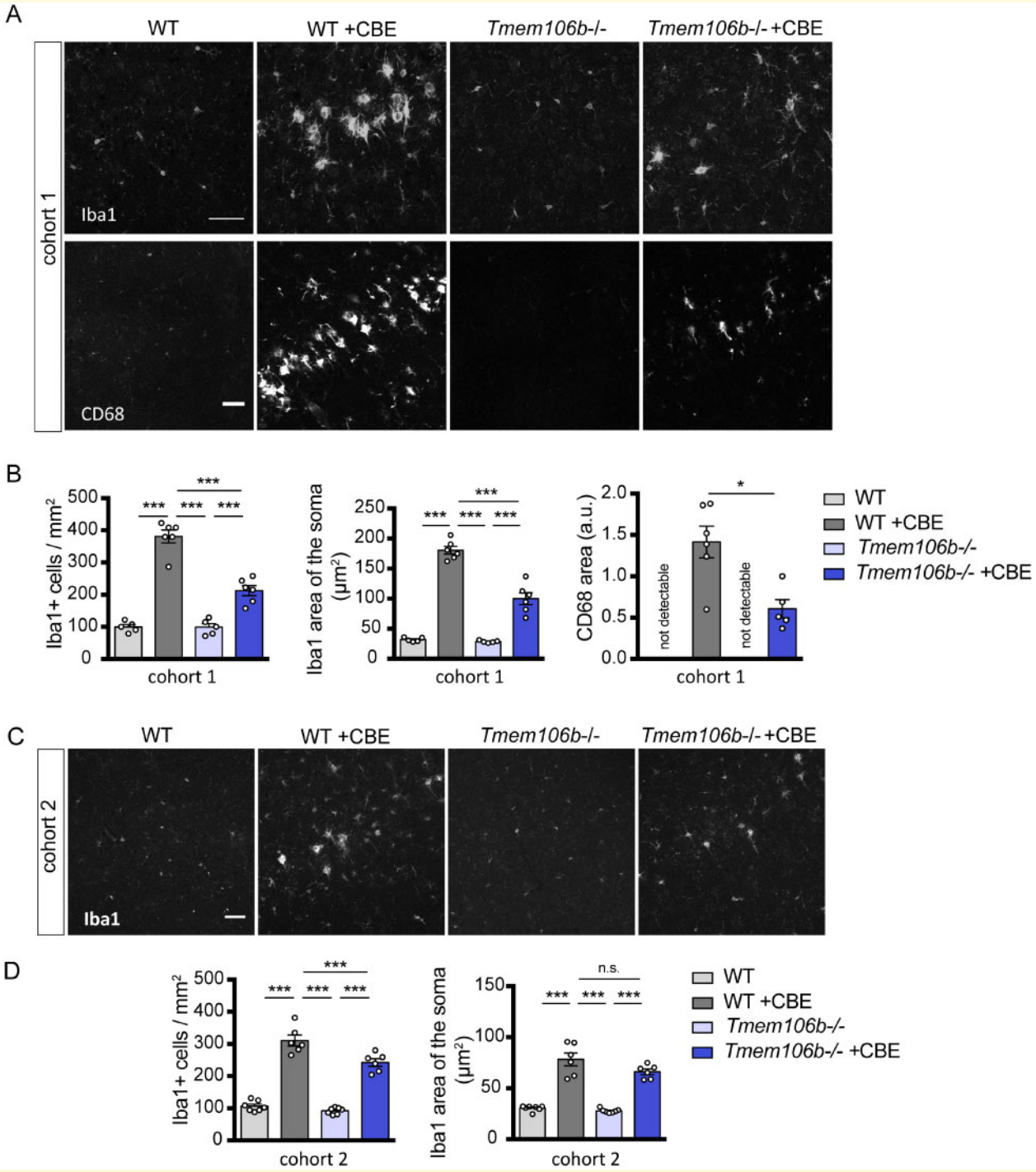

Figure 2 TMEM106B loss is protective against microgliosis induced by CBE. (**A**) Representative images of cortex in WT and *Tmem106b*−/− mice from cohort 1, treated or not with CBE, stained with anti-Iba1 and CD68 antibodies (microglia). Scale bars = 50 µm. (**B**) Graphs show mean ± SEM of number and area of the soma of Iba1+ cells and CD68+ area in the layer V of the cortex. *n* = 5–6 mice per group. (**C**) Representative images of cortex in WT and *Tmem106b*−/− mice from cohort 2, treated or not with CBE, stained with anti-Iba1 antibody (microglia). Scale bars = 50 µm. (**D**) Graphs show mean ± SEM of number and area of the soma of Iba1+ cells in the layer V of the cortex. *n* = 6–8 mice per group

colocalize with neurons (Supplementary Fig. 3C) or with microglial cells (Supplementary Fig. 3D).

Lipofuscin accumulation is a common feature of lysosomal storage disorders. In order to investigate a possible role of TMEM106B depletion in lipofuscin deposition, we measured autofluorescent signal in different brain regions of WT and *Tmem106b*−/− mice treated or not with CBE. Within the time frame of this experiment,

CBE treatment does not have a significant effect on lipofuscin accumulation in the cortex, hippocampus and thalamus in WT or *Tmem106b*−/− mice (Supplementary Fig. 4A and B).

Taken together, these results indicate that CBE treatment induces a robust astrocytosis characterized by intense Lamp1 lysosomal accumulation, which is independent of *Tmem106b* genotype. In contrast, lipofuscin accumulation is not a characteristic of this pharmacological model of GD.

TMEM106B deficiency partially rescues behavioural phenotypes induced by CBE treatment

The data above show that TMEM106B depletion rescues neurodegeneration and microgliosis, but not astrocytosis, induced by CBE. Therefore, we sought to evaluate the functional consequences by assessing motor and memory behaviour. In cohort 1, WT mice treated with CBE show a shorter latency to fall from the rotarod that the controls, indicating motor impairment, whereas *Tmem106b*−/− mice have normal motor performance independent of treatment (Fig. 3A). No further behavioural tests were conducted in this cohort due to the poor condition of some CBE-treated mice, indicating an end-stage of the disease. In cohort 2, treatment was discontinued before the appearance of pronounced motor deficits. Conduritol B epoxide-treated mice in cohort 2 did not show motor impairment in the rotarod test (data not shown), confirming an earlier stage of the disease compared to cohort 1. We decided to further explore behaviour with the open field test. Both WT and *Tmem106b*−/− mice treated with CBE travel greater distances when compared to non-treated controls (Fig. 3B), indicating hyperactivity. In order to explore whether this behaviour correlated with disinhibition, we performed the elevated plus maze test. Again, both WT and *Tmem106b*−/− mice treated with CBE show disinhibited behaviour as measured by the distance travelled in the open arms (Fig. 3C), whereas the distance travelled was similar in the closed arms (Supplementary Fig. 5). The number of entries in the open arms was also higher in CBE-treated mice than in controls (Supplementary Fig. 5). Given the neuronal loss and gliosis observed in the cortex of CBE-treated mice, we sought to investigate whether they presented cognitive impairment using the novel object recognition test. Wild-type and *Tmem106b*−/− controls prefer novelty, demonstrated by more time spent with the novel object. Interestingly, CBE-treated WT mice are unable to distinguish between novel and familiar objects and their time with each object is similar, reflecting significant memory impairment. Critically, memory performance is rescued in *Tmem106b*−/− mice exposed to CBE treatment (Fig. 3D), paralleling the rescue of neurodegeneration and microgliosis described above. These data show that the removal of TMEM106B corrects certain behavioural phenotypes in GD mice.

TMEM106B depletion accelerates Purkinje cell degeneration in *Ppt1*−/− mice

As mentioned above, null mutations in *GRN* gene cause NCL and TMEM106B deficiency compensates lysosomal, behavioural and degenerative $Grn^{-/-}$ phenotypes at early age. To study a potential role of TMEM106B in other NCL conditions, we used the genetic mouse model *Ppt1* knockout mice (*Ppt1*−/−). *Ppt1*−/− mice develop progressive motor abnormalities, autofluorescent material storage (lipofuscin) and neuronal loss, leading to early death by 10 months of age (Gupta *et al.*, 2001). Palmitoyl-protein thioesterase 1 (PPT1) is a lysosomal thioesterase that catalyzes the hydrolysis of long-chain fatty acyl CoAs. In addition to this function, PPT1 hydrolyzes fatty acids from modified cysteine residues in proteins that are undergoing degradation in the lysosome.

To investigate whether the removal of TMEM106B modulates PPT1-dependent NCL progression, we crossbred *Tmem106b*−/− mice with *Ppt1*−/− mice. Typically, *Ppt1*−/− mice show motor symptoms and brain pathology at 6 months of age (Macauley *et al.*, 2009). However, we observed some decline and early death in the double knockout *Ppt1*−/−; *Tmem106b*−/− mice starting at 4 months of age (Fig. 4A). Therefore, we collected tissue and performed histological and biochemical analyses at 5 months. First, we analysed neuronal degeneration in the cerebellum of WT, *Ppt1*−/−, *Tmem106b*−/− and double-knockout *Ppt1*−/−; *Tmem106b*−/− mice. As Purkinje cell loss is a hallmark of *Ppt1*−/− mice (Macauley *et al.*, 2009), we quantified the number of Purkinje cells in sections stained for calbindin, a canonical Purkinje cell marker. Double-knockout *Ppt1*−/−; *Tmem106b*−/− mice show significantly greater Purkinje cell loss compared to *Ppt1*−/− mice in anterior and mid-cerebellar regions, indicating an acceleration of the *Ppt1*−/− phenotype induced by TMEM106B depletion (Fig. 5A and B). We next sought to analyse the lysosomal status of the remaining Purkinje cells. Co-staining of Purkinje cells and the lysosomal protein Lamp1 revealed a significant lysosomal enlargement in both *Ppt1*−/− and double-knockout *Ppt1*−/−; *Tmem106b*−/− mice (Fig. 5C and D). In addition to the cerebellum, we further analysed neuronal death in other brain regions. NeuN staining and neuronal counting revealed a significant neuronal loss in double-knockout *Ppt1*−/−; *Tmem106b*−/− mice in the cortex (Fig. 5E and F) and CA1 region of the hippocampus (Fig. 5G and H). In line with observations in the cerebellum, a significant Lamp1-particle enlargement is also present in hippocampal CA1 neurons in both *Ppt1*−/− and double-knockout *Ppt1*−/−; *Tmem106b*−/− mice (Supplementary Fig. 6A and B),

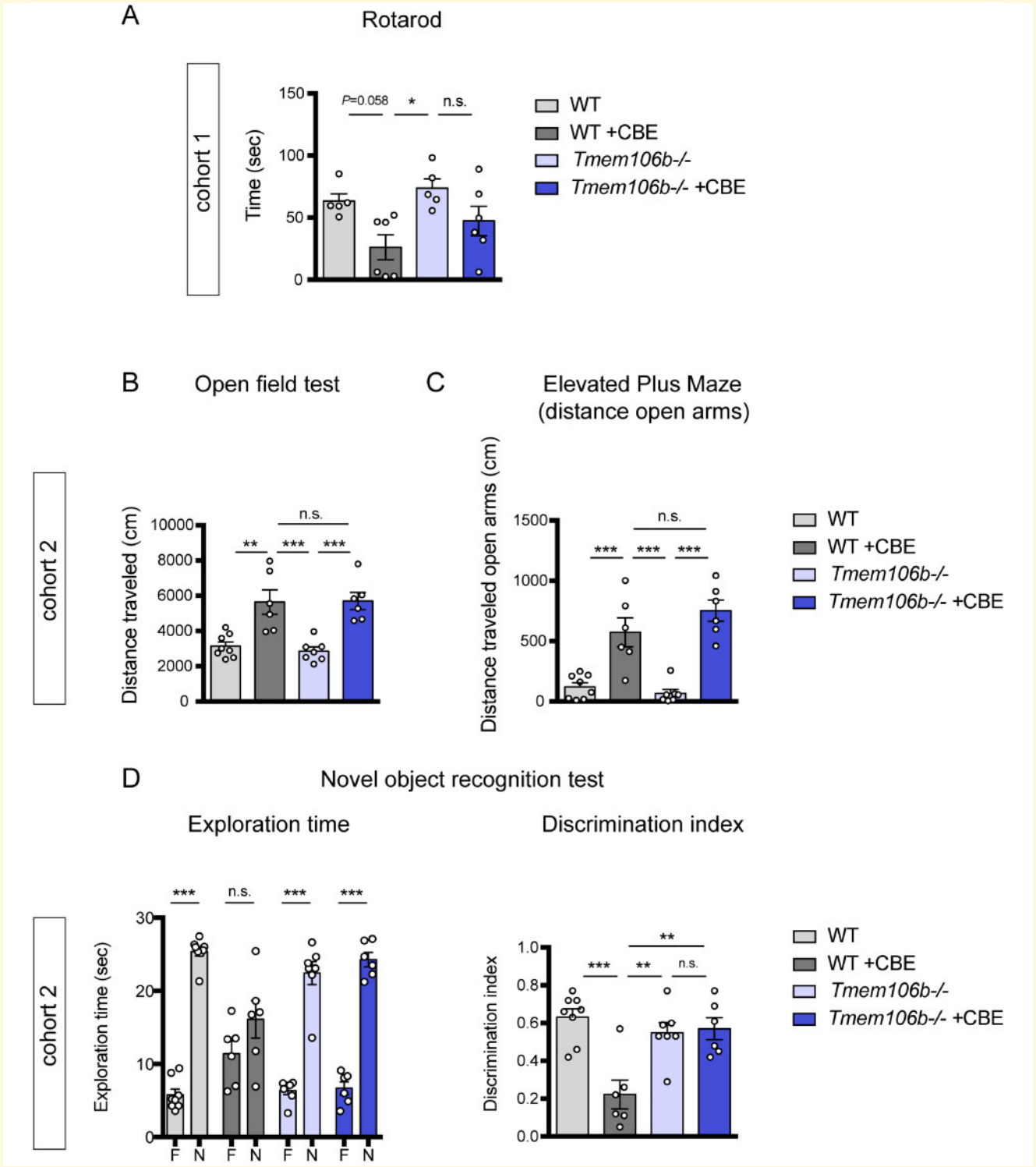

Figure 3 TMEM106B depletion protects against some behavioural phenotypes induced by CBE. (**A**) Graph shows mean ± SEM of time spent in the rotarod test in WT and *Tmem106b*−/− mice from cohort 1 treated or not with CBE. $n = 5$–6 mice per group. (**B**) Graph shows mean ± SEM of distance travelled in the open field test in WT and *Tmem106b*−/− mice from cohort 2 treated or not with CBE. $n = 6$–8 mice per group. (**C**) Graph shows mean ± SEM of distance travelled in the open arms of the elevated plus maze in WT and *Tmem106b*−/− mice from cohort 2 treated or not with CBE. $n = 6$–8 mice per group. (**D**) Graphs show mean ± SEM of exploration time of familiar (F) and novel (N) objects and discrimination index calculated as follows: (novel − familiar)/(novel + familiar); in the novel object recognition test in WT and *Tmem106b*−/− mice from cohort 2 treated or not with CBE. $n = 6$–8 mice per group

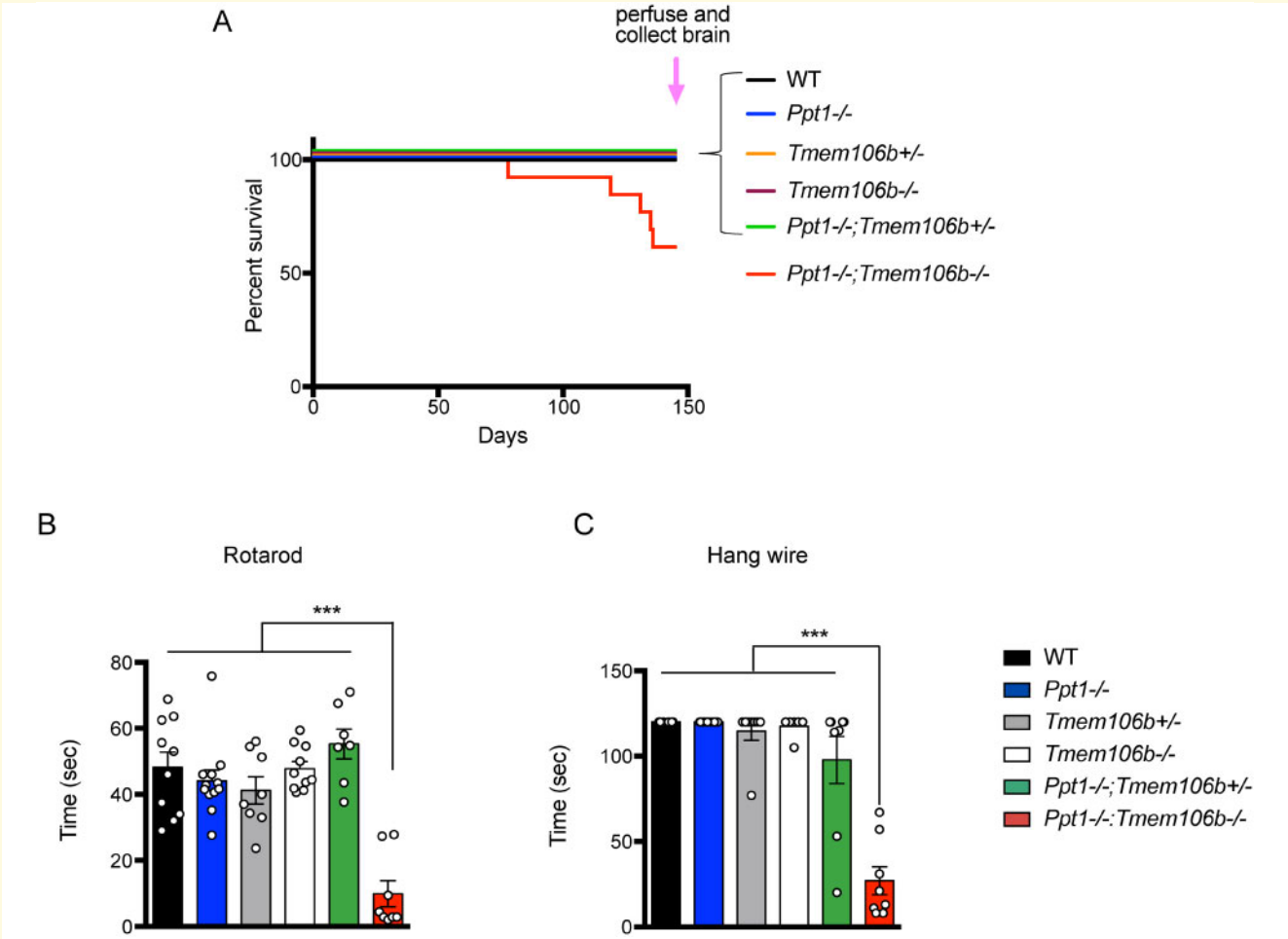

Figure 4 Loss of TMEM106B reduces survival and worsens motor phenotype in *Ppt1*−/− mice. (**A**) Survival curves of WT, *Ppt1*−/−, *Tmem106b*+/−, *Tmem106b*−/− and *Ppt1*−/−; *Tmem106b*+/− and *Ppt1*−/−; *Tmem106b*−/− mice. $n = 8$–13 mice per group. (**B**) Graph shows mean ± SEM of time spent in the Rotarod test. $n = 8$–12 mice per group. (**C**) Graph shows mean ± SEM of time until mice fell from the wire in the hang wire test. $n = 8$–12 mice per group

indicating that TMEM106B depletion does not exacerbate lysosomal accumulation. Consistent with these observations, lipofuscin accumulation (Gupta *et al.*, 2001) in different brain regions (cortex, hippocampus and cerebellum) is similarly increased in *Ppt1*−/− and double-knockout *Ppt1*−/−; *Tmem106b*−/− mice (Supplementary Fig. 7A and B). Altogether, these data show that TMEM106B deficiency accelerates Purkinje cell loss and neuronal death in the cortex and hippocampus without causing an increase in lysosomal histopathology in *Ppt1*−/− mice.

Gliosis is exacerbated in different brain regions of *Ppt1*−/− mice after TMEM106B depletion

Given that TMEM106B depletion accelerated neurodegeneration in *Ppt1*−/− mice without affecting lysosomal histopathology, we examined astrocytosis and microgliosis (Macauley *et al.*, 2009) in the cortex, hippocampus and cerebellum of double–knockout *Ppt1*−/−; *Tmem106b*−/− mice. Glial fibrillary acid protein staining shows significant astrocytosis in *Ppt1*−/− mice compared to WT and *Tmem106b*−/− controls in the different brain regions analysed. Interestingly, astrocytosis is exacerbated in double-knockout *Ppt1*−/−; *Tmem106b*−/− mice in certain brain regions (Fig. 6). Parallel to astrocyte activation, Iba1 and CD68 staining confirms significant microglia activation in *Ppt1*−/− mice. Microgliosis is also worsened by TMEM106B depletion in some brain regions (Fig. 7). Interestingly, astrocytosis and microgliosis correlate with neurodegeneration in most of the brain regions analysed, being this correlation higher in the cerebellum and hippocampus than cortex (Supplementary Fig. 8). Similar to the robust lysosomal Lamp1 signal observed within astrocytes in CBE-treated mice (Supplementary Fig. 3), *Ppt1*−/− astrocytes display substantial Lamp1 clusters (Supplementary Fig. 9A, C and

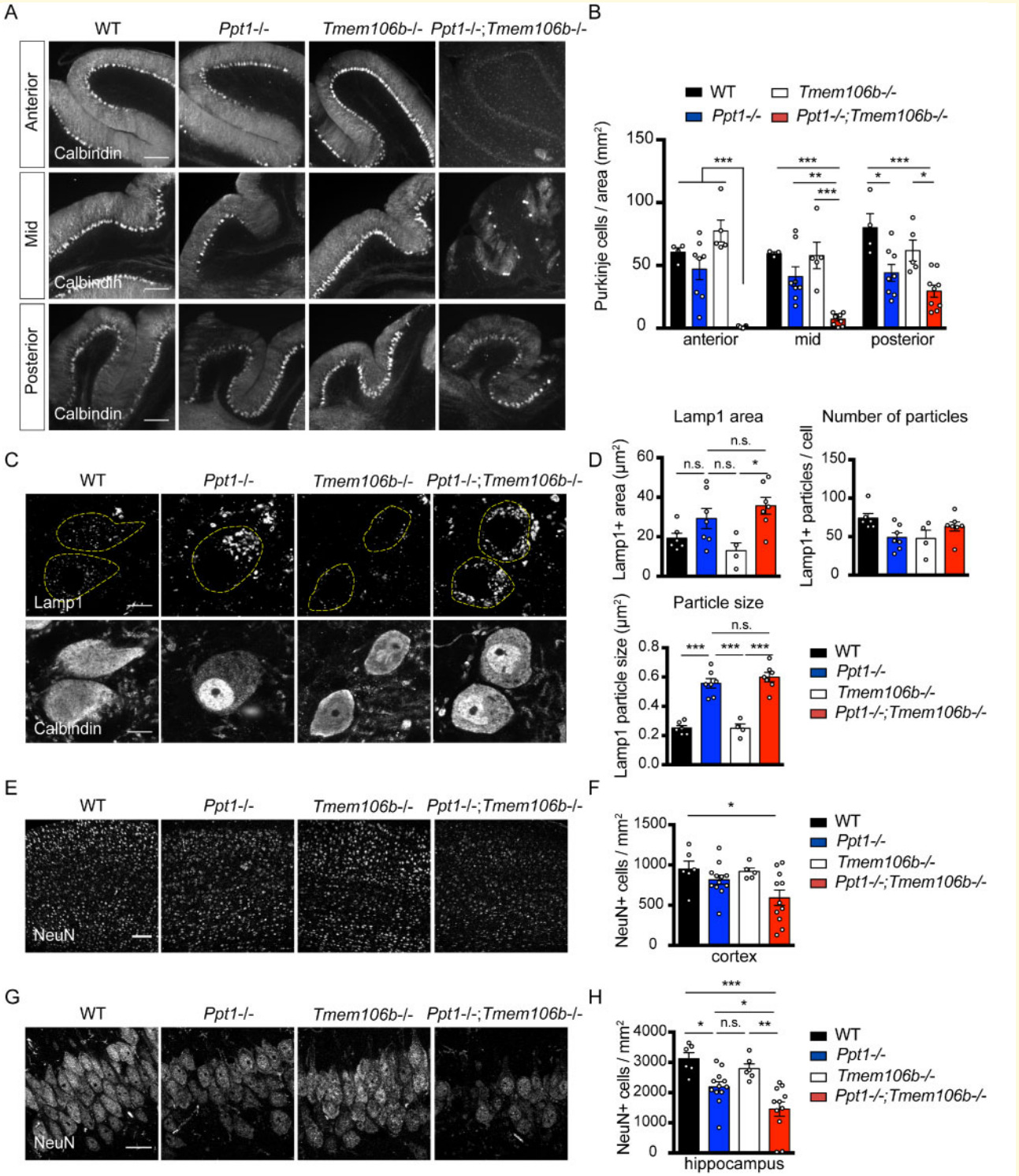

Figure 5 TMEM106B deletion accelerates neuronal death in *Ppt1*−/− mice, a model of infantile neuronal ceroid lipofuscinosis. (**A**) Representative images of anterior (I–V), mid (VI–VIII) and posterior (IX,X) cerebellar lobes stained with anti-calbindin D28k antibody in 5-month-old WT, *Ppt1*−/−, *Tmem106b*−/− and *Ppt1*−/−; *Tmem106b*−/− mice. Scale bars = 200 µm. (**B**) Graph shows mean ± SEM of number of calbindin-positive cells in the different cerebellar regions. *n* = 4–9 mice per group. (**C**) Representative images of Purkinje cells in 5-month-old WT, *Ppt1*−/−, *Tmem106b*−/− and *Ppt1*−/−; *Tmem106b*−/− mice stained with anti-Calbindin D28k and Lamp1 antibodies. Scale bar = 10 µm. *n* = 4–9 mice per group. (**D**) Graphs show mean ± SEM of Lamp1 area, number of particles and particle size in Purkinje cells. *n* = 4–7 mice per group. (**E**) Representative images of cerebral cortex in 5-month-old WT, *Ppt1*−/−, *Tmem106b*−/− and *Ppt1*−/−; *Tmem106b*−/− mice stained with anti-NeuN antibody. Scale bar = 100 µm. (**F**) Graph shows mean ± SEM of NeuN+ cells per area in the cortex. *n* = 5–12 mice per group. (**G**) Representative images of hippocampus (CA1) in 5-month-old WT, *Ppt1*−/−, *Tmem106b*−/− and *Ppt1*−/−; *Tmem106b*−/− mice stained with anti-NeuN antibody. Scale bar = 20 µm. (**H**) Graph shows mean ± SEM of NeuN+ cells per area in the hippocampus (CA1). *n* = 5–12 mice per group

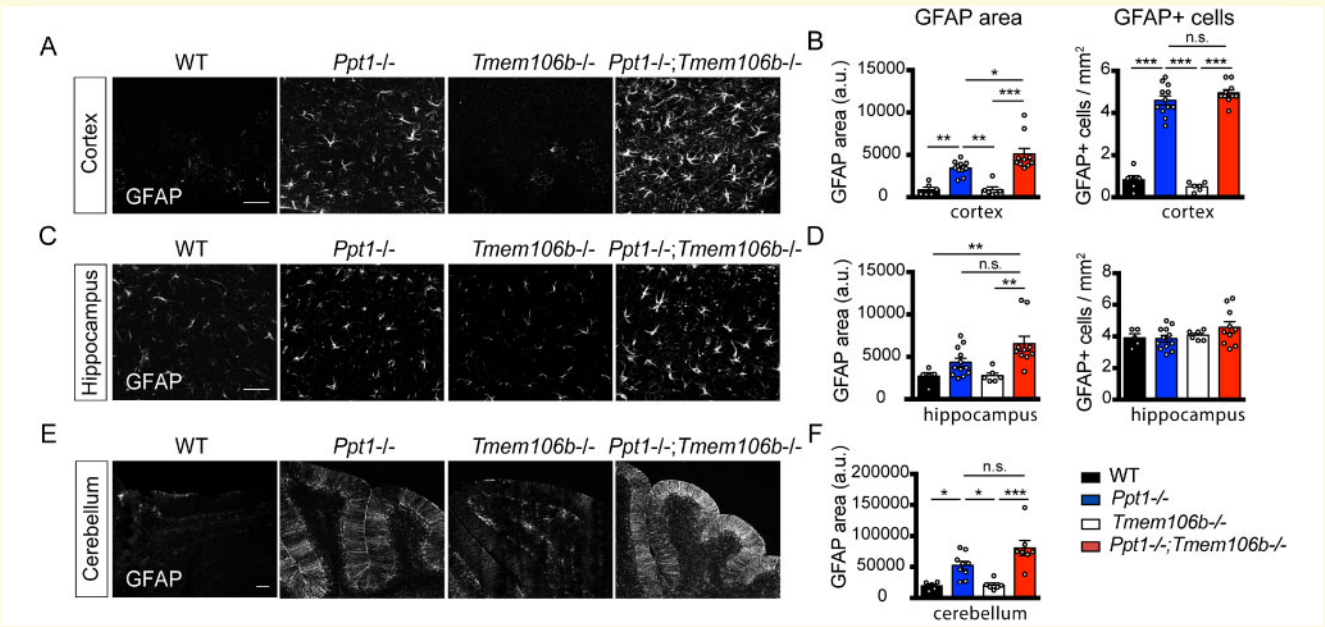

Figure 6 TMEM106B deletion exacerbates astrogliosis in the cortex of *Ppt1*−/− mice. (**A**) Representative images of cortex in 5-month-old WT, *Ppt1*−/−, *Tmem106b*−/− and *Ppt1*−/−; *Tmem106b*−/− mice stained with anti-GFAP antibody. Scale bar = 50 μm. (**B**) Graphs show mean ± SEM of number of GFAP+ cells per area (right) or GFAP+ area (left) in the cortex. *n* = 6–12 mice per group. (**C**) Representative images of hippocampus (CA1) in 5-month-old WT, *Ppt1*−/−, *Tmem106b*−/− and *Ppt1*−/−; *Tmem106b*−/− mice stained with anti-GFAP antibody. Scale bar = 50 μm. (**D**) Graphs show mean ± SEM of number of GFAP+ cells per area (right) or GFAP+ area (left) in the hippocampus. *n* = 6–12 mice per group. (**E**) Representative images of cerebellum in 5-month-old WT, *Ppt1*−/−, *Tmem106b*−/− and *Ppt1*−/−; *Tmem106b*−/− mice stained with anti-GFAP antibody. Scale bar = 100 μm. (**F**) Graph shows mean ± SEM of GFAP+ area in the cerebellum. *n* = 6–12 mice per group

D) that are not found in microglial cells (Supplementary Fig. 9B). Quantification of Lamp1 clusters within GFAP-positive cells (astrocytes) shows equal significant increase in lysosomal pathology in *Ppt1*−/− and double-knockout *Ppt1*−/−; *Tmem106b*−/− mice (Supplementary Fig. 6C and D). These results confirm that TMEM106B depletion exacerbates astrocytosis and microgliosis in several brain regions of *Ppt1*−/−, which correlate with neuronal loss.

TMEM106B loss worsens motor performance in *Ppt1*−/− mice

We next sought to evaluate whether the acceleration of neurodegeneration and gliosis in double-knockout *Ppt1*−/−; *Tmem106b*−/− mice translates into a functional decline. As described above, we observed a decrease in survival rate in double-knockout *Ppt1*−/−; *Tmem106b*−/− mice starting at around 4 months of age (Fig. 4A). At 5 months of age, *Ppt1*−/− mice do not show motor impairment in the rotarod (Fig. 4B) or wire hang (Fig. 4C) test compared to WT and *Tmem106b*−/− controls. Interestingly, double-knockout *Ppt1*−/−; *Tmem106b*−/− mice exhibit reduced latency to fall from the rotarod and wire hang test. These observations confirm the acceleration of motor impairment in *Ppt1*−/− mice driven by TMEM106B depletion.

Altered lysosomal acidification in GCase-inhibited versus PPT1 null neurons

Given the opposing effects of TMEM106B depletion in GD and NCL, we investigated the mechanisms by which TMEM106B deficiency orchestrates the divergent effects. TMEM106B protein levels are not altered in WT CBE-treated or *Ppt1*−/− mice (Supplementary Fig. 10A–D). We previously showed that TMEM106B interacts with V-ATPase and participates in lysosomal acidification (Klein *et al.*, 2017). Therefore, we imaged the acidic lysosomal compartment with the pH-sensitive dye LysoTracker red DND-99 (Chen-Plotkin *et al.*, 2012; Busch *et al.*, 2016; Fassio *et al.*, 2018). Conduritol B epoxide treatment in WT-cultured neurons significantly increases LysoTracker-positive integrated fluorescence intensity despite a comparable cell density between control and CBE-treated neurons (Fig. 8A and B). Thus, lysosomal acidification is not impaired, and appears to be enhanced after GCase inhibition. The increased LysoTracker red DND-99 staining after CBE treatment opposes the *Tmem106b*−/− neuronal phenotype (Klein *et al.*, 2017), providing a potential explanation for the rescue of some CBE phenotypes by TMEM106B deletion.

We sought to determine whether PPT1 loss might have an opposite effect to CBE treatment with regard to

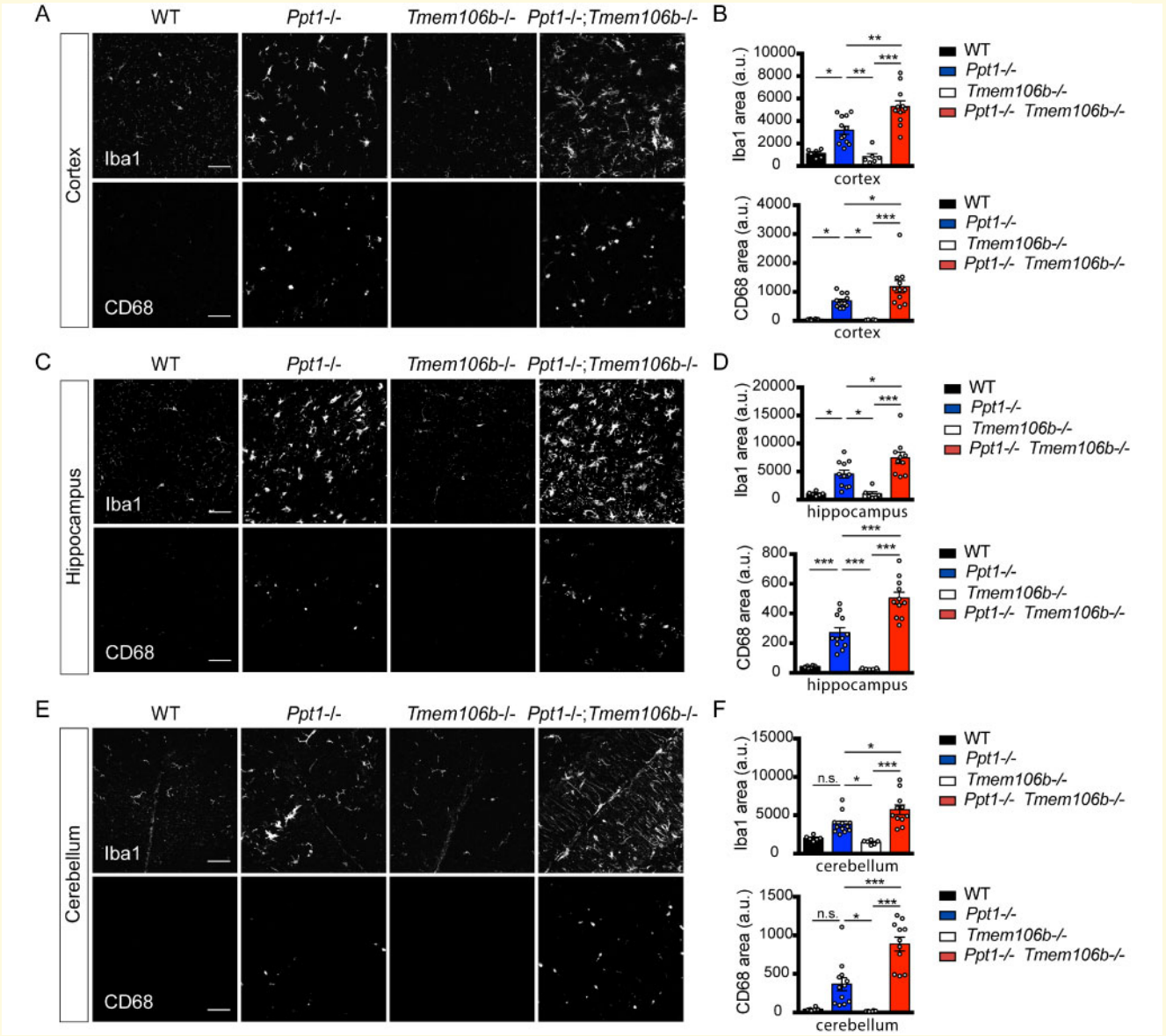

Figure 7 TMEM106B deletion exacerbates microgliosis in different brain regions in *Ppt1*−/− mice. (**A**) Representative images of cortex in 5-month-old WT, *Ppt1*−/−, *Tmem106b*−/− and *Ppt1*−/−; *Tmem106b*−/− mice stained with anti-Iba1 and CD68 antibodies. Scale bars = 50 μm. (**B**) Graphs show mean ± SEM of Iba1+ (top) or CD68+ area (bottom) in the cortex. *n* = 6–12 mice per group. (**C**) Representative images of hippocampus (CA1) in 5-month-old WT, *Ppt1*−/−, *Tmem106b*−/− and *Ppt1*−/−; *Tmem106b*−/− mice stained with anti-Iba1 and CD68 antibodies. Scale bars = 50 μm. (**D**) Graphs show mean ± SEM of Iba1+ (top) or CD68+ area (bottom) in the hippocampus. *n* = 6–12 mice per group. (**E**) Representative images of cerebellum in 5-month-old WT, *Ppt1*−/−, *Tmem106b*−/− and *Ppt1*−/−; *Tmem106b*−/− mice stained with anti-Iba1 and CD68 antibodies. Scale bars = 50 μm. (F) Graphs show mean ± SEM of Iba1+ (top) or CD68+ area (bottom) in the cerebellum. *n* = 6–12 mice per group.

lysosomal acidification. In order to study the effects of PPT1 loss specifically in neurons prior to the development of *in vivo* pathologies, we edited the *Ppt1* locus in tissue culture via CRISPR-cas9. Wild-type-cultured neurons were transduced with AAV2/1 virus expressing two single-guide (sg) RNAs against *Ppt1*. T7EI digestion confirmed *Ppt1* DNA editing (Fig. 8C) and qPCR analyses revealed a decrease in *Ppt1* mRNA with both sgRNAs (Fig. 8D). The *Ppt1* reduction via CRISPR-cas9 editing significantly reduces V-ATPase levels (Fig. 8E and F). Examination of brain tissue from *Ppt1*−/− mice revealed a similar lowering of V-ATPase levels compared to WT controls (Fig. 8G and H). These data are consistent with recent observations pointing to V-ATPase processing and trafficking alterations in *Ppt1*−/− mice (Bagh *et al.*, 2017). Therefore, we assessed the acidic lysosome

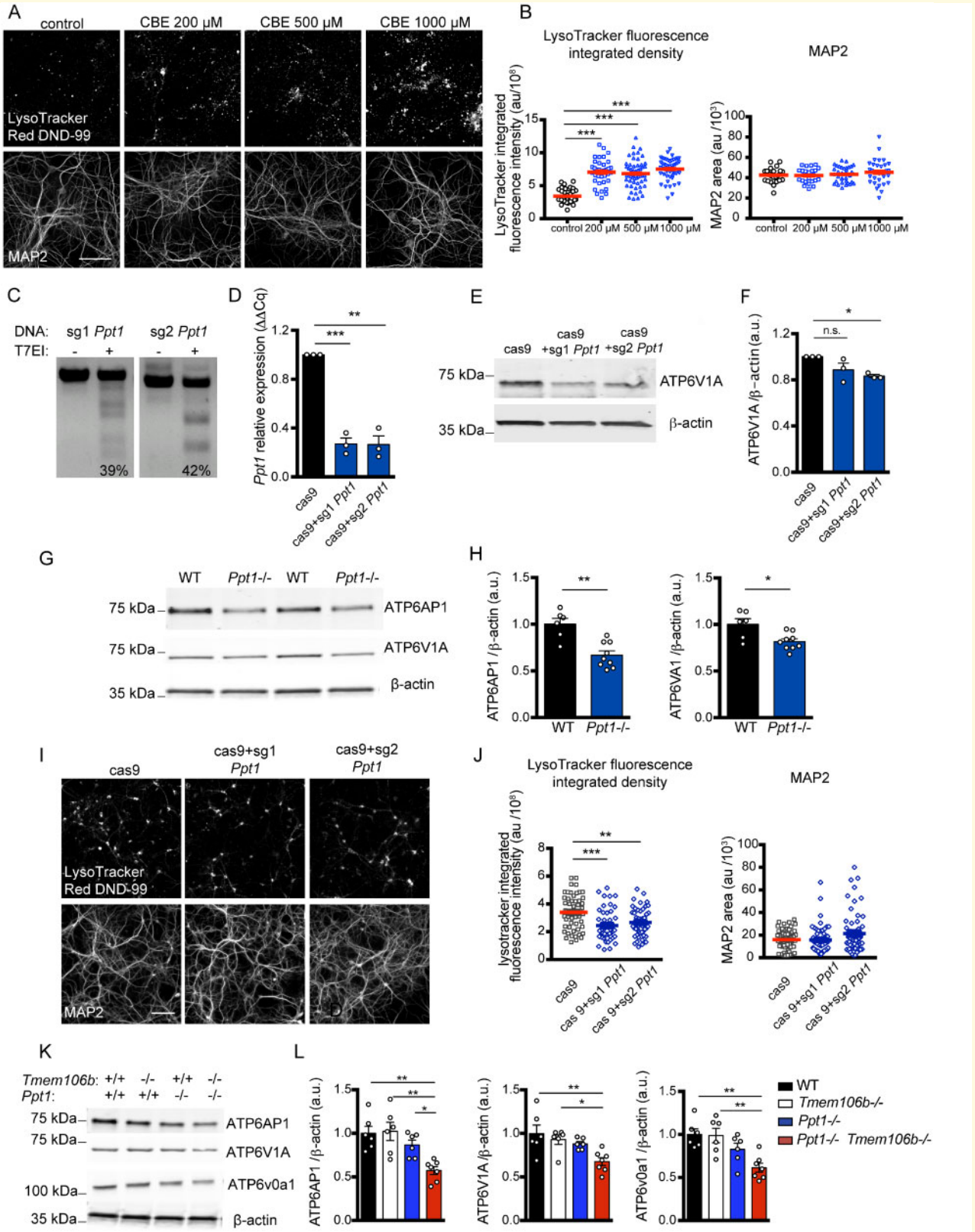

Figure 8 Opposite effect of CBE and PPT1 deficiency on lysosomal acidification. (**A**) Representative images of primary cortical cultured neurons treated with CBE for 7 days at different concentrations and stained with anti-MAP2 antibody and LysoTracker Red DND-99. Scale bar = 50 µm. (**B**) Graphs show mean ± SEM LysoTracker-red-DND-99-integrated fluorescence intensity and MAP2-positive area from one representative experiment. $n = 36–54$ images. (**C**) Representative agarose gel showing confirmation of *Ppt1* DNA editing by T7EI digestion in cultured neurons 2 weeks after AAV2/1 infection. Cortical cultured neurons were infected with AAV2/1 expressing two single-guide *Ppt1* RNA sequences (sg) at 3 DIV. (**D**) *Ppt1* mRNA expression in cultured neurons 2 weeks after AAV2/1 infection. $n = 3$ independent experiments.

(continued)

compartment of PPT1-deficient neurons. *Ppt1* down-regulation with CRISPR-cas9 editing in neurons leads to significant reduction in LysoTracker red DND-99-positive area, suggesting impairment in lysosomal acidification in the absence of PPT1 (Fig. 8I and J). Significant reduction in V-ATPase subunits was also observed in cortical brain extracts from double-knockout *Ppt1*−/−; *Tmem106b*−/− mice (Fig. 8K and L).

These results support the hypothesis that CBE-induced alterations in lysosomal acidification are partially counteracted by TMEM106B depletion, similar to the interaction of TMEM106B and PGRN deficiencies (Klein *et al.*, 2017). On the other hand, PPT1 deficiency destabilizes V-ATPase levels, causing a lysosomal acidification deficit that is further exacerbated by TMEM106B depletion.

Discussion

The major finding of this study is that TMEM106B deficiency rescues neurodegeneration in a GD model while exacerbating neurodegeneration in a PPT1-dependent NCL model. The GD rescue by TMEM106B deletion parallels a previous study in PGRN-dependent neurodegeneration (Klein *et al.*, 2017). The rescue of GD-related neurodegeneration is accompanied by improved memory and motor function, as well as a reversal of microgliosis, despite continued astrocytosis and disinhibition behaviour. A distinguishing feature of the different neurodegenerative conditions is their effect on V-ATPase levels and lysosomal pH. For GCase inhibition, the acidic lysosomal compartment is increased, and the consequences are counteracted by TMEM106B loss, which suppresses V-ATPase (Klein *et al.*, 2017). For PPT1 neuronal deficiency, V-ATPase levels are suppressed and this is exacerbated by TMEM106B deficiency. Overall, these studies reveal a modulating effect of the TMEM106B/V-ATPase interaction on neurodegeneration, with the net benefit or detriment of TMEM106B loss varying as a function of V-ATPase function in different neurodegenerative conditions.

For the GD model, the rescuing effect of TMEM106B loss was restricted to neurodegeneration, microgliosis, memory and motor function, but not astrocytosis or disinhibition. This suggests differences in GCase-dependent cellular dysfunction for neurons and astrocytes. Interestingly, some type 1 GD (non-neuronopathic) patients show astrogliosis without significant neuronal loss (Wong *et al.*, 2004). The astrocytic phenotype of the CBE-treated mice included striking LAMP1-positive lysosomal rings. Although the basis of this cellular morphology will require future studies, it is not TMEM106B dependent. In the PPT1 model, astrocytosis is affected by TMEM106B loss to the same extent as microgliosis and neurodegeneration. Thus, the TMEM106B independence of astrocyte pathology is unique to the GD model.

The reduced memory, motor and microglial phenotypes in CBE-treated *Tmem106b*−/− mice may be secondary to neuronal sparing. Although sustained microglial activation is observed in patients with GD and in mouse models of the disease, the role that microglial cells play in GD is not well understood. Traditionally, microglia have been considered harmful in several neurodegenerative diseases due to cytokine release and neuroinflammation. However, recent data indicate that microglial cells can perform different tasks and function in both positive and negative ways in different mouse disease models (Song and Colonna, 2018). A GD mouse model with GCase deficiency restricted to neuronal and glial precursors and their progeny, but not to microglia, shows symptoms similar to those observed in mice with reduced GCase activity in all tissues except the skin but with a slower phenotypic progression (Enquist *et al.*, 2007). Both models present neuronal loss and microgliosis, supporting the idea that GCase function is critical for neuronal survival. In addition, these results suggest that GCase-deficient microglia may not be the primary determinants of the central nervous system pathogenesis in GCase-deficient mice, but they contribute by influencing the onset and progression of the disease (Enquist *et al.*, 2007). Conversely, a previous study has shown that GCase deficiency in dopaminergic neurons is not sufficient to induce neurodegeneration, but it causes sustained microglia activation, pointing to GCase deficiency in other cell types as a potential pathological mechanism (Soria *et al.*, 2017). A cytotoxic role for microglia is also suggested after a critical threshold of glucosylceramide storage is reached in neurons, inducing the release of inflammatory cytokines by microglia that amplifies the inflammatory response and contributes to neuronal death (Vitner *et al.*, 2012). Further studies are needed in order to clarify the role of microglia in neurodegeneration in GD.

(**E**) Representative immunoblots with anti-ATP6V1A and β-actin using cortical cultured neuronal lysates 2 weeks after AAV2/1 infection. Full blots for this other panels are shown in Supplementary Fig. 11. (**F**) Graph shows mean ± SEM of the immunoblot signal from **E**. $n = 3$ independent experiments. (**G**) Representative immunoblots with anti-ATP6AP1, ATP6V1A and β-actin using cortical lysates from WT and *Ppt1*−/− mice. (**H**) Graphs show mean ± SEM of the immunoblot signal from **G**. $n = 6$–9 mice per group. (**I**) Representative images of primary cortical cultured neurons infected with AAV2/1. Two weeks later, neurons were stained with anti-MAP2 antibody and LysoTracker Red DND-99. Scale bar = 100 μm. (**J**) Graphs show mean ± SEM LysoTracker-red-DND-99-integrated fluorescence intensity and MAP2-positive area from one representative experiment. $n = 50$–58 images. (**K**) Representative immunoblots with anti-ATP6AP1, ATP6V1A and ATPv0a1 and β-actin using cerebral cortex lysates from 5-month-old WT, *Ppt1*−/−, *Tmem106b*−/− and *Ppt1*−/−; *Tmem106b*−/− mice. (**L**) Graphs show mean ± SEM of the immunoblot signal from **K**. $n = 6$–7 mice per group

Deficiency of several different lysosomal genes can result in NCL, including PPT1 and PGRN. Despite shared NCL neuropathology (Ward *et al.*, 2017), certain aspects of PGRN-dependent neurodegeneration are rescued by TMEM106B loss (Klein *et al.*, 2017), whereas PPT1-dependent neurodegeneration is strongly exacerbated. These conditions share lipofuscinosis, but the presence of lipofuscin does not correlate with outcome, consistent with the notion that the accumulated proteolipid itself is not directly responsible for degeneration. This is consistent with the observation of lipofuscin in healthy aged brain without neurodegeneration (Moreno-García *et al.*, 2018).

The opposite effects of TMEM106B deficiency in the GD and PPT1-NCL models are striking, but are also present in the PGRN–deficient state. For example, PGRN-null lipofuscinosis is not rescued by TMEM106B deficiency, whereas retinal neurodegeneration, behavioural deficits and lysosomal dysregulation are reversed in young adult mice (Klein *et al.*, 2017). In addition, after 11 months of age, double-knockout *Grn−/−; Tmem106b−/−* mice develop synthetic phenotypes with brainstem and spinal cord gliosis coupled to weakness and ataxia leading to poor feeding and death (Zhou *et al.*, 2020a). These opposing effects are consistent with TMEM106B modulating a pathway such as lysosomal acidification that participates differentially in various degenerative mechanisms and at different disease stages. Importantly, these phenotypes are all manifest with low levels of residual TMEM106B protein in hypomorphic *Tmem106b−/−* mice. TMEM106B protein levels have non-linear effect, such that experimentally complete loss of TMEM106B and PGRN leads to a severe and earlier lysosomal deficits and neurodegeneration in spinal cord (Feng *et al.*, 2020a; Zhou *et al.*, 2020a). Partial reduction of TMEM106B may have greater relevance to common variants of *TMEM106B* in humans and any prospects for TMEM106B-directed therapeutic approaches.

Previously, we found that TMEM106B physically associates with subunits of V-ATPase, including subunit AP1, and participates in maintaining expression levels of V-ATPase and lysosomal acidification. The dysregulation of V-ATPase and lysosomal pH predicts the opposing action of TMEM106B null state on neurodegeneration in GD and PPT1-dependent NCL. For the GCase inhibition model of GD, the acidic lysosome compartment of neurons is enhanced, and V-ATPase is not lost even with neurodegeneration. As for PGRN deficiency, TMEM106B reduction has neurodegeneration-rescuing effect. In contrast, PPT1 deficiency leads to a reduction in V-ATPase and impairment of lysosomal acidification, which is exacerbated by TMEM106B deletion. Thus, disease-specific changes in lysosomal pH and V-ATPase level appear to predict whether the effect of reduced V-ATPase caused by TMEM106B deletion corrects a deficit or moves lysosomal pH further from normal with degenerative consequences.

In this study and previously, we have considered the role of *TMEM106B* in lysosomal storage disorders and FTLD, but the gene is implicated genetically in other degenerative conditions, including Alzheimer's Disease. Hippocampal sclerosis is negatively associated with the FTLD-protective *TMEM106B* allele. The linkage of GCase heterozygosity with PD risk implies that TMEM106B loss-of-function may ameliorate PD as well.

The mechanistic studies implicating TMEM106B ability to maintain steady-state protein levels of V-ATPase and lysosomal acidification suggest a potential therapeutic intervention site. Pharmacological agents blocking the TMEM106B interaction with V-ATPase, or partially reducing the catalytic function of the V-ATPase itself, are predicted to mimic TMEM106B reduction. In this sense, such compounds may have therapeutic utility to reduce neurodegeneration in PGRN deficiency, GCase deficiency, Alzheimer's Disease and PD. For the neurodegeneration of PPT1 deficiency, the same compounds or other agents with V-ATPase inhibiting activity may be deleterious. Overall, our molecular studies of TMEM106B provide new insights into disease-specific neurodegenerative mechanisms.

Supplementary material

Supplementary material is available at *Brain Communications* online.

Acknowledgement

The authors thank Dr. Sreeganga Chandra for providing *Ppt1−/−* mice.

Funding

This study was supported by research grants from the N.I.A., N.I.N.D.S. and the Falk Medical Research Trust to S.M.S.

Competing interests

The authors report no competing interests.

References

Arrant AE, Roth JR, Boyle NR, Kashyap SN, Hoffmann MQ, Murchison CF, et al. Impaired β-glucocerebrosidase activity and processing in frontotemporal dementia due to progranulin mutations. Acta Neuropathol Commun 2019; 7: 218.

Bagh MB, Peng S, Chandra G, Zhang Z, Singh SP, Pattabiraman N, et al. Misrouting of v-ATPase subunit V0a1 dysregulates lysosomal acidification in a neurodegenerative lysosomal storage disease model. Nat Commun 2017; 8: 14612.

Busch JI, Martinez-Lage M, Ashbridge E, Grossman M, Van Deerlin VM, Hu F, et al. Expression of TMEM106B, the frontotemporal lobar degeneration-associated protein, in normal and diseased human brain. Acta Neuropathol Commun 2013; 1: 36.

Busch JI, Unger TL, Jain N, Skrinak RT, Charan RA, Chen-Plotkin AS. Increased expression of the frontotemporal dementia risk factor TMEM106B causes C9orf72-dependent alterations in lysosomes. Hum Mol Genet 2016; 25: 2681–2697. ddw127.

Česen M, Pegan K, Špes A, Turk B. Lysosomal pathways to cell death and their therapeutic applications. Exp Cell Res 2012; 318: 1245–51.

Chen-Plotkin AS, Unger TL, Gallagher MD, Bill E, Kwong LK, Volpicelli-Daley L, et al. TMEM106B, the risk gene for frontotemporal dementia, is regulated by the microRNA-132/212 cluster and affects progranulin pathways. J Neurosci 2012; 32: 11213–27.

Cox TM, Schofield JP. 3 Gaucher's disease: clinical features and natural history. Baillières Clin Haematol 1997; 10: 657–89.

Enquist IB, Bianco CL, Ooka A, Nilsson E, Mansson J-E, Ehinger M, et al. Murine models of acute neuronopathic Gaucher disease. Proc Natl Acad Sci USA 2007; 104: 17483–8.

Farfel-Becker T, Vitner EB, Futerman AH. Animal models for Gaucher disease research. Dis Model Mech 2011; 4: 746–52.

Fassio A, Esposito A, Kato M, Saitsu H, Mei D, Marini C, C4RCD Research Group, et al. De novo mutations of the ATP6V1A gene cause developmental encephalopathy with epilepsy. Brain 2018; 141: 1703–18.

Feng T, Mai S, Roscoe JM, Sheng RR, Ullah M, Zhang J, et al. Loss of TMEM 106B and PGRN leads to severe lysosomal abnormalities and neurodegeneration in mice [Internet]. EMBO Rep 2020a; 21: e50219. Available from: https://onlinelibrary.wiley.com/doi/abs/10.15252/embr.202050219 (11 November 2020, date last accessed).

Feng T, Sheng RR, Solé-Domènech S, Ullah M, Zhou X, Mendoza CS, et al. A role of the frontotemporal lobar degeneration risk factor TMEM106B in myelination. Brain 2020b; 143: 2255–71.

Finch N, Carrasquillo MM, Baker M, Rutherford NJ, Coppola G, DeJesus-Hernandez M, et al. TMEM106B regulates progranulin levels and the penetrance of FTLD in GRN mutation carriers. Neurology 2011; 76: 467–74.

Ghavami S, Shojaei S, Yeganeh B, Ande SR, Jangamreddy JR, Mehrpour M, et al. Autophagy and apoptosis dysfunction in neurodegenerative disorders. Prog Neurobiol 2014; 112: 24–49.

Gupta P, Soyombo AA, Atashband A, Wisniewski KE, Shelton JM, Richardson JA, et al. Disruption of PPT1 or PPT2 causes neuronal ceroid lipofuscinosis in knockout mice. Proc Natl Acad Sci USA 2001; 98: 13566–71.

Hafler BP, Klein ZA, Jimmy Zhou Z, Strittmatter SM. Progressive retinal degeneration and accumulation of autofluorescent lipopigments in progranulin deficient mice. Brain Res 2014; 1588: 168–74.

Hruska KS, LaMarca ME, Scott CR, Sidransky E. Gaucher disease: mutation and polymorphism spectrum in the glucocerebrosidase gene (GBA). Hum Mutat 2008; 29: 567–83.

Hu F, Padukkavidana T, Vægter CB, Brady OA, Zheng Y, Mackenzie IR, et al. Sortilin-mediated endocytosis determines levels of the frontotemporal dementia protein. Progranulin Neuron 2010; 68: 654–67.

Jian J, Zhao S, Tian Q-Y, Liu H, Zhao Y, Chen W-C, et al. Association between progranulin and Gaucher disease. EBioMedicine 2016a; 11: 127–37.

Jian J, Tian Q-Y, Hettinghouse A, Zhao S, Liu H, Wei J, et al. Progranulin recruits HSP70 to β-glucocerebrosidase and is therapeutic against Gaucher disease. EBioMedicine 2016b; 13: 212–24.

Kanfer JN, Legler G, Sullivan J, Raghavan SS, Mumford RA. The Gaucher mouse. Biochem Biophys Res Commun 1975; 67: 85–90.

Klein ZA, Takahashi H, Ma M, Stagi M, Zhou M, Lam TT, et al. Loss of TMEM106B ameliorates lysosomal and frontotemporal dementia-related phenotypes in progranulin-deficient mice. Neuron 2017; 95: 281–96.e6.

Konermann S, Brigham MD, Trevino AE, Hsu PD, Heidenreich M, Cong Le, et al. Optical control of mammalian endogenous transcription and epigenetic states. Nature 2013; 500: 472–6.

Lang CM, Fellerer K, Schwenk BM, Kuhn P-H, Kremmer E, Edbauer D, et al. Membrane orientation and subcellular localization of transmembrane protein 106B (TMEM106B), a major risk factor for frontotemporal lobar degeneration. J Biol Chem 2012; 287: 19355–65.

Lüningschrör P, Werner G, Stroobants S, Kakuta S, Dombert B, Sinske D, et al. The FTLD risk factor TMEM106B regulates the transport of lysosomes at the axon initial segment of motoneurons. Cell Rep 2020; 30: 3506–19.e6.

Macauley SL, Wozniak DF, Kielar C, Tan Y, Cooper JD, Sands MS. Cerebellar pathology and motor deficits in the palmitoyl protein thioesterase 1-deficient mouse. Exp Neurol 2009; 217: 124–35.

Menzies FM, Fleming A, Rubinsztein DC. Compromised autophagy and neurodegenerative diseases. Nat Rev Neurosci 2015; 16: 345–57.

Moreno-García A, Kun A, Calero O, Medina M, Calero M. An overview of the role of lipofuscin in age-related neurodegeneration. Front Neurosci 2018; 12: 464.

Murray ME, Cannon A, Graff-Radford NR, Liesinger AM, Rutherford NJ, Ross OA, et al. Differential clinicopathologic and genetic features of late-onset amnestic dementias. Acta Neuropathol 2014; 128: 411–21.

Nelson PT, Wang W-X, Partch AB, Monsell SE, Valladares O, Ellingson SR, et al. Reassessment of risk genotypes (*GRN*, *TMEM106B*, and *ABCC9* Variants) associated with hippocampal sclerosis of aging pathology. J Neuropathol Exp Neurol 2015; 74: 75–84.

Nicholson AM, Rademakers R. What we know about TMEM106B in neurodegeneration. Acta Neuropathol 2016; 132: 639–51.

Nixon RA. The role of autophagy in neurodegenerative disease. Nat Med 2013; 19: 983–97.

Nixon RA, Yang D-S. Autophagy and neuronal cell death in neurological disorders. Cold Spring Harb Perspect Biol 2012; 4: a008839.

Rocha EM, Smith GA, Park E, Cao H, Graham A-R, Brown E, et al. Sustained systemic glucocerebrosidase inhibition induces brain α-synuclein aggregation, microglia and complement C1q activation in mice. Antioxid Redox Signal 2015; 23: 550–64.

Rutherford NJ, Carrasquillo MM, Li M, Bisceglio G, Menke J, Josephs KA, et al. TMEM106B risk variant is implicated in the pathologic presentation of Alzheimer disease. Neurology 2012; 79: 717–8.

Salazar SV, Gallardo C, Kaufman AC, Herber CS, Haas LT, Robinson S, et al. Conditional deletion of *Prnp* rescues behavioral and synaptic deficits after disease onset in transgenic Alzheimer's disease. J Neurosci 2017; 37: 9207–21.

Schnell SA, Staines WA, Wessendorf MW. Reduction of lipofuscin-like autofluorescence in fluorescently labeled tissue. J Histochem Cytochem 1999; 47: 719–30.

Schwenk BM, Lang CM, Hogl S, Tahirovic S, Orozco D, Rentzsch K, et al. The FTLD risk factor TMEM106B and MAP6 control dendritic trafficking of lysosomes. Embo J 2013; 33: 450–67.

Simons C, Dyment D, Bent SJ, Crawford J, D'Hooghe M, Kohlschütter A, Care4Rare Consortium, et al. A recurrent de novo mutation in TMEM106B causes hypomyelinating leukodystrophy. Brain 2017; 140: 3105–11.

Smith KR, Damiano J, Franceschetti S, Carpenter S, Canafoglia L, Morbin M, et al. Strikingly different clinicopathological phenotypes determined by progranulin-mutation dosage. Am J Hum Genet 2012; 90: 1102–7.

Song WM, Colonna M. The identity and function of microglia in neurodegeneration. Nat Immunol 2018; 19: 1048–58.

Soria FN, Engeln M, Martinez-Vicente M, Glangetas C, López-González MJ, Dovero S, et al. Glucocerebrosidase deficiency in dopaminergic neurons induces microglial activation without neurodegeneration. Hum Mol Genet 2017; 26: 2603–15.

Stagi M, Klein ZA, Gould TJ, Bewersdorf J, Strittmatter SM. Lysosome size, motility and stress response regulated by fronto-temporal dementia modifier TMEM106B. Mol Cell Neurosci 2014; 61: 226–40.

Swiech L, Heidenreich M, Banerjee A, Habib N, Li Y, Trombetta J, et al. In vivo interrogation of gene function in the mammalian brain using CRISPR-Cas9. Nat Biotechnol 2015; 33: 102–6.

Takahashi H, Klein ZA, Bhagat SM, Kaufman AC, Kostylev MA, Ikezu T, For the Alzheimer's Disease Neuroimaging Initiative, et al. Opposing effects of progranulin deficiency on amyloid and tau pathologies via microglial TYROBP network. Acta Neuropathol 2017; 133: 785–807.

Tropea TF, Mak J, Guo MH, Xie SX, Suh E, Rick J, et al. *TMEM106B* Effect on cognition in Parkinson disease and frontotemporal dementia. Ann Neurol 2019; 85: 801–11.

Valdez C, Ysselstein D, Young TJ, Zheng J, Krainc D. Progranulin mutations result in impaired processing of prosaposin and reduced glucocerebrosidase activity. Hum Mol Genet 2019; 29: 716–26. ddz229.

Van Deerlin VM, Sleiman PMA, Martinez-Lage M, Chen-Plotkin A, Wang L-S, Graff-Radford NR, et al. Common variants at 7p21 are associated with frontotemporal lobar degeneration with TDP-43 inclusions. Nat Genet 2010; 42: 234–9.

Vieira RT. Epidemiology of early-onset dementia: a review of the literature. Clin Pract Epidemiol Ment Health 013; 9: 88–95.

Vitner EB, Farfel-Becker T, Eilam R, Biton I, Futerman AH. Contribution of brain inflammation to neuronal cell death in neuronopathic forms of Gaucher's disease. Brain 2012; 135: 1724–35.

Vitner EB, Futerman AH. Neuronal forms of Gaucher disease. In: E Gulbins, I Petrache, editors. Sphingolipids in disease. Vienna: Springer Vienna; 2013. p. 405–19.

Vitner EB, Salomon R, Farfel-Becker T, Meshcheriakova A, Ali M, Klein AD, et al. RIPK3 as a potential therapeutic target for Gaucher's disease. Nat Med 2014; 20: 204–8.

Vitner EB, Vardi A, Cox TM, Futerman AH. Emerging therapeutic targets for Gaucher disease. Expert Opin Ther Targets 2015; 19: 321–34.

Ward ME, Chen R, Huang H-Y, Ludwig C, Telpoukhovskaia M, Taubes A, et al. Individuals with progranulin haploinsufficiency exhibit features of neuronal ceroid lipofuscinosis. Sci Transl Med 2017; 9: eaah5642.

Wong K, Sidransky E, Verma A, Mixon T, Sandberg GD, Wakefield LK, et al. Neuropathology provides clues to the pathophysiology of Gaucher disease. Mol Genet Metab 2004; 82: 192–207.

Zhou X, Brooks M, Jiang P, Koga S, Zuberi AR, Baker MC, et al. Loss of Tmem106b exacerbates FTLD pathologies and causes motor deficits in progranulin-deficient mice [Internet]. EMBO Rep 2020a; 21: e50197. Available from: https://onlinelibrary.wiley.com/doi/abs/10.15252/embr.202050197 (11 November 2020, date last accessed).

Zhou X, Nicholson AM, Ren Y, Brooks M, Jiang P, Zuberi A, et al. Loss of TMEM106B leads to myelination deficits: implications for frontotemporal dementia treatment strategies. Brain 2020b; 143: 1905–19.